Article

Amazon forest biogeography predicts resilience and vulnerability to drought

https://doi.org/10.1038/s41586-024-07568-w

Received: 28 November 2022

Accepted: 15 May 2024

Published online: 19 June 2024

Check for updates

Shuli Chen[1]✉, Scott C. Stark[2], Antonio Donato Nobre[3], Luz Adriana Cuartas[4], Diogo de Jesus Amore[4], Natalia Restrepo-Coupe[1,5], Marielle N. Smith[2,6], Rutuja Chitra-Tarak[7], Hongseok Ko[1], Bruce W. Nelson[8] & Scott R. Saleska[1,9]✉

Amazonia contains the most extensive tropical forests on Earth, but Amazon carbon sinks of atmospheric CO_2 are declining, as deforestation and climate-change-associated droughts[1–4] threaten to push these forests past a tipping point towards collapse[5–8]. Forests exhibit complex drought responses, indicating both resilience (photosynthetic greening) and vulnerability (browning and tree mortality), that are difficult to explain by climate variation alone[9–17]. Here we combine remotely sensed photosynthetic indices with ground-measured tree demography to identify mechanisms underlying drought resilience/vulnerability in different intact forest ecotopes[18,19] (defined by water-table depth, soil fertility and texture, and vegetation characteristics). In higher-fertility southern Amazonia, drought response was structured by water-table depth, with resilient greening in shallow-water-table forests (where greater water availability heightened response to excess sunlight), contrasting with vulnerability (browning and excess tree mortality) over deeper water tables. Notably, the resilience of shallow-water-table forest weakened as drought lengthened. By contrast, lower-fertility northern Amazonia, with slower-growing but hardier trees (or, alternatively, tall forests, with deep-rooted water access), supported more-drought-resilient forests independent of water-table depth. This functional biogeography of drought response provides a framework for conservation decisions and improved predictions of heterogeneous forest responses to future climate changes, warning that Amazonia's most productive forests are also at greatest risk, and that longer/more frequent droughts are undermining multiple ecohydrological strategies and capacities for Amazon forest resilience.

Three 'once in a century' droughts (Extended Data Fig. 1a–c) occurred in the Amazon basin over a single decade—in 2005, 2010 and 2015–2016[20,21]—provoking multiple forest responses that are difficult to explain (Fig. 1 and Extended Data Fig. 1d–f). For example, unexpected overall increases (green-up) in remotely sensed canopy greenness (a proxy for photosynthetic function) during the 2005 drought[9,10] (Fig. 1a and Extended Data Fig. 1a,d) appear at odds with reports of simultaneous carbon losses from increased tree mortality observed in ground plots[16]. Furthermore, the 2005 green-up contrasts with a strong decrease in greenness (brown-down) during the 2010 drought[11] (Fig. 1b and Extended Data Fig. 1e), while the 2015/2016 El Niño, the largest and most intense drought of the three, provoked an intermediate response that also included substantial green-up regions (Fig. 1c and Extended Data Fig. 1f). Climate drivers alone, although important[10], are evidently insufficient to predict the complexity of drought responses across heterogeneous landscapes[22]. Still missing is a general understanding of what drives differences in drought resilience across Amazonian landscapes, a 'functional biogeography'[23] of forest drought response that can address the question of why some forests (or times) are resilient (exhibiting green-up or reduced mortality), while others are vulnerable (exhibiting brown-down or enhanced mortality).

Here we used satellite indices of forest photosynthesis to test whether three non-exclusive ecological hypotheses that go beyond climate-only explanations, developed from forest plot-scale observations, can also predict regional scale responses to these recent droughts across intact terra firme forest types of the Amazon basin.

The first (other side of drought[24]) hypothesis is that shallow-water-table hydrological environments[25] provide trees with greater access to water resources, making them more drought resilient (as observed in forest plots near Manaus[26,27]), than trees in forests over deep water tables, of which the mortality rates typically increase with drought[2,16]. This hypothesis predicts that shallow-water-table forests should show less brown-down (or even experience green-up with reduced anoxia or

[1]Department of Ecology and Evolutionary Biology, University of Arizona, Tucson, AZ, USA. [2]Department of Forestry, Michigan State University, East Lansing, MI, USA. [3]National Institute for Space Research (INPE), São José dos Campos, Brazil. [4]National Center for Monitoring and Early Warning of Natural Disasters (CEMADEN), São José dos Campos, Brazil. [5]Cupoazu LLC, Etobicoke, Ontario, Canada. [6]School of Environmental and Natural Sciences, College of Science and Engineering, Bangor University, Bangor, UK. [7]Los Alamos National Laboratory, Earth and Environmental Sciences, Los Alamos, NM, USA. [8]Brazil's National Institute for Amazon Research (INPA), Manaus, Brazil. [9]Department of Environmental Sciences, University of Arizona, Tucson, AZ, USA. ✉e-mail: slchen@arizona.edu; saleska@arizona.edu

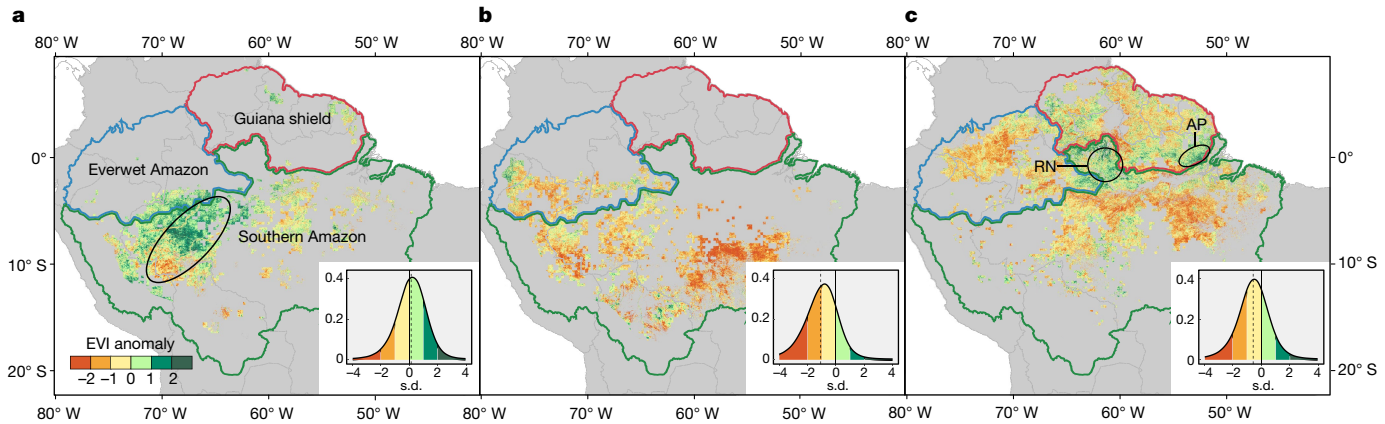

Fig. 1 | Amazon forest remotely sensed responses to droughts. **a**–**c**, Amazon forest remotely sensed responses to the droughts of 2005 (**a**), 2010 (**b**) and 2015/2016 (**c**), expressed as standardized anomalies of multiangle implementation of atmospheric correction (MAIAC) EVI (a proxy of photosynthetic capacity) in drought-affected pixels (defined in Extended Data Fig. 1a–c). Note that **a** highlights an ellipse of green-up and brown-down patterns that correspond to shallow and deep water tables in Fig. 2a; **c** highlights two areas exhibiting green-up—RN, in the Rio Negro catchment and AP in Amapa state—for comparison to Figs. 4 and 5. Insets show the frequency distributions of MAIAC EVI anomalies in drought regions for droughts in 2005 (+0.14, $P < 0.001$, d.f. = 916) (**a**), 2010 (−1.06, $P < 0.001$, d.f. = 1,057) (**b**) and 2015 (−0.57, $P < 0.001$, d.f. = 2218) (**c**). Statistical analysis was performed using Student's two-sided *t*-tests, whereby, after the variogram analysis (see Methods, 'Variogram analysis for removal of spatial autocorrelation'), the degrees of freedom (d.f. = $n - 1$) were adjusted for spatial autocorrelation based on n = number of statistically independent 0.4° × 0.4° drought-affected pixels in each drought region; all P values are significantly less than the Bonferroni correction for three comparisons $\alpha = 0.05/3 = 0.016$.

more sunlight due to reduced cloud cover during drought) compared with forests with deep water tables.

The second (soil fertility) hypothesis[28,29] is that, in more-fertile forests, where tree growth and turnover rates are high, fast-growing trees that invest less in drought tolerance have a competitive advantage over trees that invest more. This is because it is easier to simply regrow trees cheaply when resources are plentiful, especially when tree-killing droughts are rare. This hypothesis therefore predicts that more-fertile forests will exhibit greater drought susceptibility (more brown-down or less green-up) compared with less fertile forests.

The third (rooting depth/traits) hypothesis focuses on the role of tree characteristics themselves. This hypothesis predicts that forests dominated by species with either drought avoidance traits (tall, deeply rooted trees)[30–33] or drought tolerance traits (high wood density or embolism-resistant xylem)[29,34–36] are more drought tolerant, even over deep water tables.

These three dimensions (water-table depth, soil fertility and vegetation properties) define an 'ecotope space', within which different forest ecotopes are located and may interact with and respond to climate in different ways. To the extent that such responses are predictably structured by ecotopes (which also vary by geographical region within the Amazon; Extended Data Fig. 2), it should be possible to derive a unified functional biogeography of the basin-wide diversity of forest drought responses.

We tested these hypotheses using satellite indices of photosynthetic capacity (the enhanced vegetation index (EVI), corrected for view- and illumination-geometry artifacts)[37] and of photosynthetic activity (the Global OCO-2 solar induced fluorescence product (GOSIF))[38]. We focused on drought-affected regions, defined as those of which the maximum cumulative water deficit (MCWD; see Methods, 'Climate anomalies for drought definition and mapping') reached more than 1 s.d. below the mean of the remote sensing record (from 2000 to 2020)[39]. Vegetation index anomalies during drought were analysed as a function of water-table depth (as captured by height above nearest drainage (HAND))[25] and of gridded climate data (photosynthetically active radiation (PAR), vapour pressure deficit (VPD) and precipitation) derived from remote-sensing platforms (see Methods, 'Drought resilience and vegetation anomalies'; Extended Data Fig. 3).

We took the relative green-up (more positive or less negative vegetation anomalies) as an index of resilient photosynthetic capacity or activity because it suggests that there are more carbon resources for responding to stress and, notably, is predictive of outcomes on the ground that are commonly associated with resilience at the individual-tree scale (lower mortality, greater growth and greater xylem embolism resistance; see Methods, 'Drought resilience and vegetation anomalies').

Southern Amazon forest drought response

Focusing first on the locale of the 2005 drought (in the southern Amazon, one of three regions identified in Methods, 'Classification of forest regions according to ecotopes'; Extended Data Fig. 4), we found substantial structuring of the 2005 greening by water-table depth across the drought-impacted region. This is visually evident in the spatial correspondence of 2005 forest green-up/brown-down regions (Fig. 1a (ellipse)) with shallow/deep-water-table forests (Fig. 2a (ellipse)), and is quantified by bin-averaged EVI (Fig. 2b) and GOSIF (Extended Data Fig. 1g (green symbols/lines)) observations versus water-table depth. Vegetation green-up in 2005 was concentrated in pixels with shallow water tables but, as water tables deepened, positive vegetation index greening anomalies decreased and then reversed to become negative anomalies (Fig. 2b and Extended Data Fig. 1g). Notably, the strongest 2005 green-up was in forests that experienced the strongest drought (Fig. 2b (dark orange points)), apparently because these areas experienced a greater frequency of excess sunlight (Fig. 2c (histograms)), which was particularly advantageous to shallow-water-table forests (Fig. 2c (blue-hued lines)).

To rigorously quantify the sensitivity of forest response across multiple droughts, we implemented two complementary statistical analytical frameworks: nonlinear multiple regression (using generalized additive modelling (GAM)), to test our three hypotheses based on their ability to best predict basin-wide drought anomalies[40] (see Methods, 'AIC-selected GAMs for hypothesis testing and prediction'), and structural causal modelling (SCM) to formally quantify causal effects of the different environmental predictors selected by the GAM analysis[41] (see Methods, 'SCM using DAG'). Both modelling approaches were conducted on a 0.4° grid, the resolution needed to avoid inflation of statistical significance by accounting for spatial autocorrelation among nearby pixels (see Methods, 'Variogram analysis for removal of spatial

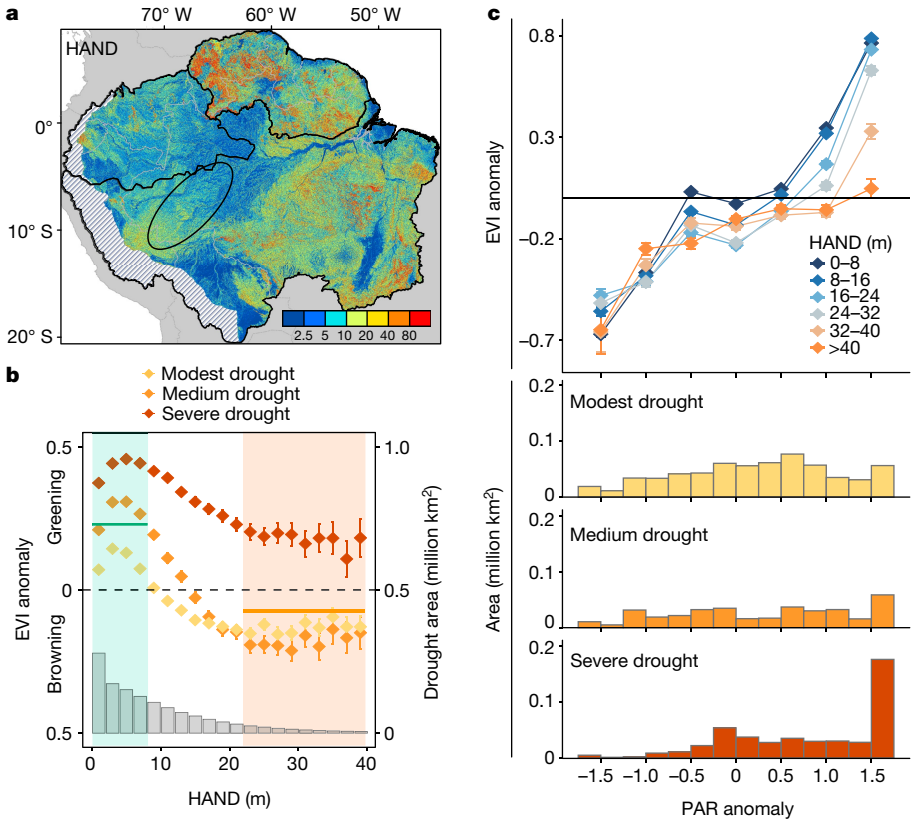

Fig. 2 | The Amazon forest response to the 2005 drought is structured by water-table depth. a, Water-table depth map (indexed by HAND in metres, Andes excluded[25]) with an ellipse highlighting shallow and deep water tables that correspond to green-up and brown-down patterns in Fig. 1a. **b**, Observed EVI anomalies (from Fig. 1a) bin-averaged by water-table depth (HAND) (±95% confidence interval (CI)), and by modest (n = 566,848), medium (n = 334,148) and severe (n = 443,000) drought 1 km pixels (those with drought index MCWD of 1–1.5 s.d., 1.5–2 s.d. and >2 s.d. below the mean, respectively). An area histogram of drought-affected HAND (right axis) is shown. The average EVI anomaly across all severities (horizontal lines) for shallow-water-table forests (0–8 m, green band) and deep-water-table forests (>22 m, orange band) is shown. **c**, Observed EVI anomalies (from Fig. 1a) bin-averaged by PAR anomalies (±95% CI), and by different water-table depths (HAND values) (top; n = 1,461,118 total 1 km pixels). Bottom, histograms of PAR anomaly according to drought severity.

autocorrelation'; Supplementary Fig. 1). As the two approaches largely converged, we report the GAM predictive modelling results here, and provide comparisons with the SCM results in the Methods (Methods, 'Comparing inferences from SCM with predictive GAM regressions').

When all three droughts were modelled simultaneously within Southern Amazonia, using GAM to also account for the effects of climate (Supplementary Table 1a), we found that, despite large differences observed in responses among the years (Fig. 1a–c), the overall other-side-of-drought (hypothesis 1) prediction of a negative relationship between remotely sensed vegetation anomalies and deepening water tables observed in 2005 was consistently confirmed across all three droughts in this region (Fig. 3a). Notably, although there was an almost universal browning response to the 2010 drought (Fig. 1b), vegetation anomalies remained significantly structured by water-table depth (Fig. 3a (purple symbols/lines)).

This analysis suggests that the ability of shallow-water-table forests (but not of deep) to respond positively to excess sunlight (possibly including relief from anoxia[24]) was a key general (multi-drought) mechanism of southern Amazon forest drought response (Fig. 3b (coloured curves)). Interdrought differences in climate drivers—not differences in the water-table depth distribution of impacted areas (Fig. 3a; distributions did not differ much)—accounted for much of the interdrought differences in forest response (in Fig. 3a, the observed points correspond well with the model predictions, which differ among droughts only due to climate). Notably, PAR increased during the 2005 and 2015/2016 droughts (Fig. 3b (distributions) and Extended Data Fig. 3j,l), promoting green-up, but decreased during the 2010 drought (due in part to excess smoke aerosols from high fire rates[42]; Fig. 3b (distribution) and Extended Data Fig. 3k). Anomalously high VPD across the droughted region in 2010 (Extended Data Fig. 3n versus Extended Data Fig. 3m,o) may also have contributed to reduced green-up/increased brown-down in 2010.

Importantly, interdrought differences in southern Amazon forest responses were mediated by drought length (Fig. 3c; as hypothesized previously[24]). Despite the even greater sunlight increases in 2015 than in 2005 (Fig. 3b (histograms)), the overall green-up in 2015/2016 was less than in 2005 (Fig. 3a), apparently due to the exceptional length of the latter drought (Fig. 3c (distribution)). Initial green-up in shallow-water-table-forests (Fig. 3c (blue lines)) reversed to brown-down in regions experiencing drought for longer than 3 months, with increasingly stronger brown-down the longer the drought. Sufficiently long droughts therefore probably deplete shallow water tables, diminishing and then reversing their protective effect.

The contrasting responses between shallow and deep-water-table forests of the southern Amazon support the other-side-of-drought' (hypothesis 1) and, at the same time, help to reconcile the much-discussed apparent disagreement between remote-sensing studies showing 2005 drought-associated green-up on average[9,10] (interpreted as showing forest resilience to or even benefit from drought) and ground-based plot studies showing 2005 drought-associated excess in tree mortality on average[16] (interpreted as showing forest vulnerability to drought). However, our more-fine-grained analysis suggests that the excess greening and the excess mortality were not in the same places; it is the locales with shallow-water-table forests that were benefited by drought, while deep-water-table forests are vulnerable—a consistent pattern revealed by both remote sensing (Figs. 2b and 3a) and ground-based forest demography (tree mortality drought response increases with water-table depth; Fig. 3d). The apparent disagreement arises because the published plot-based sampling efforts[2,16] are not random, but skewed towards the deeper-water-table regions that experienced brown-down during drought (Figs. 2b and 3e (orange shaded regions)), while the basin as a whole has more shallow-water-table forests like those that experienced greening (Figs. 2b and 3e (green-shaded regions)) (half of the Amazon basin). Shallow water tables may therefore gain (or lose less) carbon during drought (as seen previously[27]), partially offsetting the more negative effect of drought seen on forest mortality and carbon balance in deeper-water-table forests[2,16].

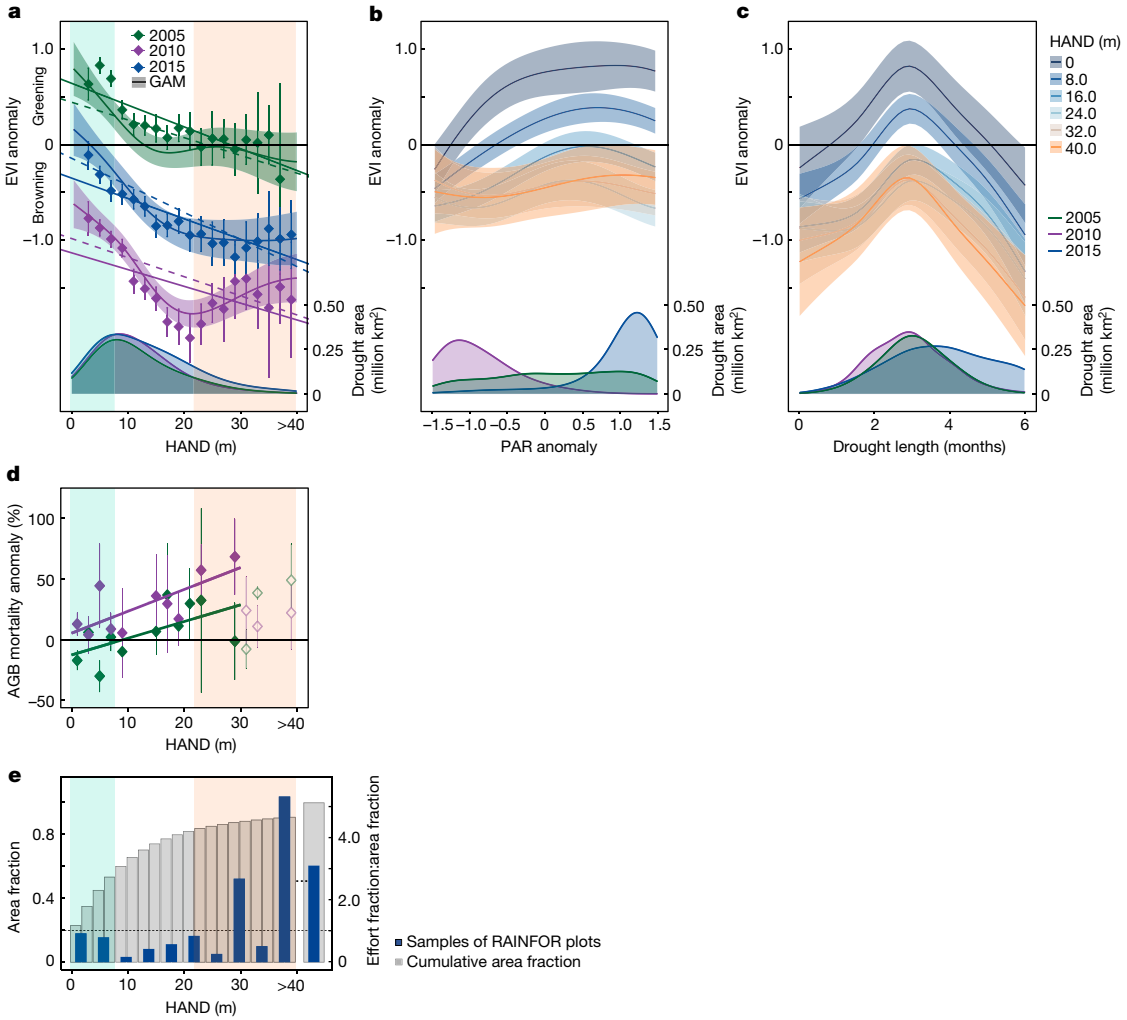

Fig. 3 | Southern Amazon forest responses to multiple droughts. a, Climate-adjusted EVI responses versus HAND water-table depths support the other-side-of-drought hypothesis (hypothesis 1) (with negative slopes) for observations (bin averages ± 95% CI, solid regression line) and GAM predictions (±95% confidence shaded region, dashed regression line) for 2005 (green, slope = −0.019 ± 0.001 s.e. m^{-1}), 2010 (purple, slope = −0.020 ± 0.002 s.e. m^{-1}) and 2015 (blue, slope = −0.028 ± 0.002 s.e. m^{-1}) droughts, each paired with HAND distributions. **b**, HAND-specific PAR sensitivity of GAM-predicted EVI responses (±95% CI shaded region), paired with PAR anomaly distributions (right axis), show greater sensitivity for shallower water tables. **c**, HAND-specific drought-length sensitivity of GAM-predicted EVI responses (±95% CI shaded region), paired with drought-duration distributions (months) (right axis), show shallow-water-table protection declining after 3 months. Climate-adjusted responses use GAM and drought-specific median climate to predict responses or adjust observations. **d**, Aboveground biomass (AGB) mortality responses (mortality-associated carbon flux; the percentage deviation from long-term MgC ha^{-1} yr^{-1} in ground plots)[2] versus HAND (average of plots within each HAND bin, ±95% CI, regression line for depths less than 30 m) support hypothesis 1 (with consistent positive slopes) for the 2005 (green, slope = 1.4% m^{-1}, $P = 0.051$) and 2010 (purple, linear regression slope = 1.8% m^{-1}, $P = 0.015$) droughts (**d**). **e**, Distributions of cumulative basin-wide HAND area (grey bars, left axis), and of ground-based sampling effort per HAND interval, normalized to the proportion of the basin area (plot area × years monitored, per HAND interval, divided by fractional basin area per HAND interval, giving the effort per interval relative to 1.0) (blue bars, right axis). This shows that ground sampling efforts under-represent prevalent shallow-water-table forests that greened up (green band, around 55% of the basin, but 16% of the effort) and over-represent deep-water-table forests that browned down (orange band, about 20% of the basin but 55% of the effort).

Basin-wide forest drought response

Although we observed consistent support for the other-side-of-drought hypothesis (hypothesis 1) across both time (three droughts) and space in southern Amazon forests (Fig. 3a) (separately confirmed by causal modelling analysis; Extended Data Fig. 6e), we found consistently opposite drought responses with water-table depth (EVI anomalies increased with water-table depth) in the ever-wet Amazon of the northwest and in the lower-fertility Guiana Shield in the northeast (see Extended Data Fig. 5, in which fertility is quantified as exchangeable base cations[43]). These observations falsify hypothesis 1 outside the southern Amazon. We next used forest responses to the 2015/2016 drought (the only drought large enough to substantially impact large portions of all three regions of the basin simultaneously) to test whether joint consideration of all three hypotheses together could explain the biogeography of forest drought response across the basin as a whole.

When gridded ecotope factors (soil fertility and texture[43,44] and vegetation properties such as canopy height[34,45]) were included as predictors in our GAM analyses for the 2015/2016 drought (Fig. 4 and Supplementary Table 1d), coherent differences between southern and northern Amazon regions emerged from interacting effects of water-table depth (hypothesis 1)[24], soil fertility (hypothesis 2)[28,29] and tree rooting depth (hypothesis 3, using forest canopy height as a rough proxy for rooting depth when water tables are deep, consistent with limited observations of tree-height–rooting-depth relationships[31–33,46]).

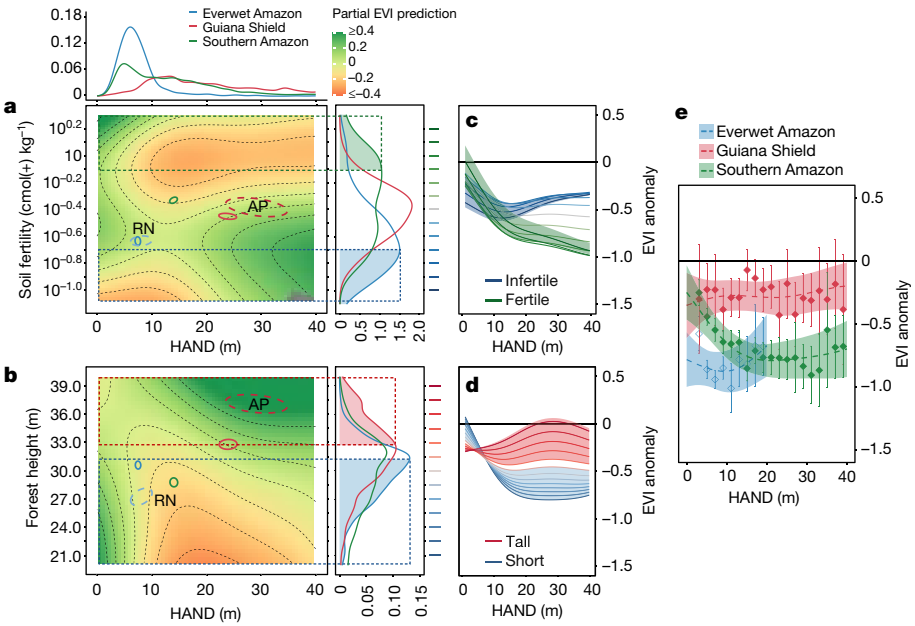

Fig. 4 | Basin-wide Amazon forest responses to the 2015 drought, structured by ecotopes and predicted by whole-basin GAM analysis. a,**b**, GAM partial predictions of EVI anomalies (colour scale) for soil fertility[43] (vertical axis) and HAND[25] (horizontal axis) terms only (**a**), and for forest height[45] and HAND[25] terms only (**b**). Ecotope distributions in southern, everwet and Guiana Shield forests (**a**, top right and **b**, right), and associated 99% confidence ellipses (main graph). The mean values of two areas exhibiting green-up in Fig. 1c (RN, in Rio Negro catchment, and AP in Amapa state) illustrate differing mechanisms of green-up (especially evident in **b**, where tall trees, despite deep water tables, promote green-up in AP, while shallow water tables promote green-up for RN). **c**,**d**, Adjusted EVI anomaly versus HAND with increasing fertility (blue to green shaded areas, corresponding to coloured areas in the tails of the fertility distribution in **a**, right) (**c**) or forest height (blue to red shaded areas, corresponding to coloured areas in the tails of the forest height distribution in **b**, right) (**d**). **e**, Region-specific EVI anomaly sensitivities to HAND, comparing adjusted observations (bin averages ± 95% CI, n = 636, 668 and 1,792 0.4° pixels for the everwet, Guiana Shield and southern Amazon regions, respectively) to adjusted GAM predictions (lines and 95% confidence shaded area). Note that adjusted EVI anomalies indicate that climate and ecotope factors not displayed in the graph are held constant at basin-wide (**a**–**d**) or regional average (**e**) values. See Supplementary Table 1d.

The effect of water-table depth on drought response across regions depended on soil fertility (Fig. 4a): highly fertile areas most strongly evinced the protective effect of shallow water tables (Fig. 4a (green portion of the fertility distribution, corresponding to the green lines in Fig. 4c)), while lower-fertility areas were either less affected by water-table depth or showed the opposite response pattern (Fig. 4a (blue portion of the fertility distribution, corresponding to the blue lines in Fig. 4c)). This is consistent with hypothesis 2[28,29] that, as soil nutrients become more limiting, trees invest in drought-resistance traits (for example, high xylem embolism resistance), and with observations of strong association between regions of low soil fertility and high wood density (Supplementary Table 2). We also noted interactions of water-table depth with soil texture (Extended Data Fig. 7a), as discussed in Methods, 'AIC-selected GAMs for hypothesis testing and prediction' (2).

The effect of water-table depth on drought response also depended on forest height (Fig. 4b), with the tallest forests, which are expected to have deeper rooting zones, enabling green-up even in regions (like the Guiana Shield) with deeper water tables (Fig. 4b (red portion of the forest height distribution, corresponding to the red lines in Fig. 4d)). Meanwhile, taller forests performed worse than shorter tree forests in shallow-water-table areas (Fig. 4d and Extended Data Fig. 6h (red versus blue lines)), consistent with findings that, when lacking a deep-root advantage, tall trees may experience higher drought mortality due to greater exposure to atmospheric drought (high VPD)[47]. Deep water tables may promote deep-rooted tall trees with resilience to seasonal atmospheric and soil water deficit exposure, with access to more consistently available deep soil water, enabling them (like shallow rooted trees over shallow water tables) to take advantage of extra sunlight during moderate droughts.

An empirical test of the basin-wide model predictions (Fig. 4a–d) showed that the fully integrated analysis accounting for the differences in the ecotope factors in different regions (Extended Data Fig. 2) was able to consistently predict the different kinds of drought responses observed in different regions of the basin (Fig. 4e).

Our GAM modelling framework, paired with causal inference modelling, generates a rich suite of testable hypotheses for future research into forest drought response (see Methods, 'Testing alternative interpretations and considering caveats'). These address such questions as: (1) whether coarse-scale patterns (like those deriving from the 1–40 km pixels used here) may emerge from such mechanisms as access to water tables, which vary across landscapes, from forest plateaus to adjacent valleys, at fine scales of just a few metres (Extended Data Fig. 8); (2) whether individual relatively tall trees may be at greater drought risk (as shown by some studies[48,49]) even within tall forests of which the average height is here predicted to be more protective against drought than shorter forests; (3) whether forests are more sensitive to droughts that occur in wet versus dry seasons (Extended Data Fig. 7b–d); (4) the effects of forest degradation on drought sensitivity; and generally, of whether these mechanisms apply in other ecosystem types in the Amazon basin and beyond.

Functional biogeography of Amazon drought

We used the GAM predictions (Fig. 4) of different drought responses across different forest ecotopes (here defined by water-table depth, soil fertility and texture, and forest height) to map a biogeography of forest drought resilience (where resilient pixels, as defined in Methods, 'Drought resilience and vegetation anomalies', are those in which ecotope factors promote relative green-up) and vulnerability (pixels

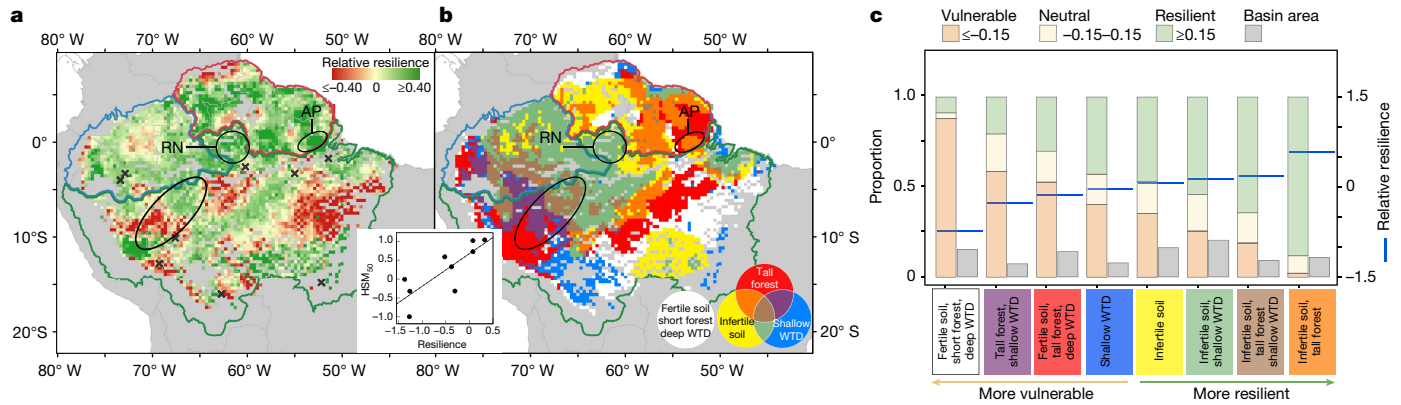

Fig. 5 | A biogeography of Amazon forest drought resilience and vulnerability. a, Regions that are relatively more resilient (likely to exhibit EVI green-up) (green) or more vulnerable (red) to drought, based on standardized GAM drought response predictions of EVI anomaly from ecotope factors only (from Fig. 4 and Supplementary Table 1d; removing the effects of climate variability by setting climate equal to its basin-wide average (Methods, 'Deriving the basin-wide biogeography of forest drought resilience/vulnerability')). Crosses indicate validation sites where remote-sensing-derived resilience predicts plot-based physiological drought tolerance (tree hydraulic safety margins (HSMs); Methods, 'Forest plot data'), as seen in the inset (linear regression $R^2 = 0.65$; $P = 0.008$, $n = 9$ plots). **b**, Overlapping strategies and ecotopes structuring the distribution of relative drought resilience mapped in **a**, as promoted by the presence of resilience factors: shallow water table depth (WTD), indexed by HAND < 10 m (blue), low-fertility soils (cation concentrations $< 10^{-0.35}$ cmol(+) kg^{-1}, yellow) or tall deep-rooted trees (heights > 32.5 m, red), with overlap indicated by the primary colour mixing rules in the legend, and white indicating no resilience factor (which, notably, corresponds well to the most vulnerable red regions in **a**). **c**, The distribution of resilience factor groups, and the proportion of relatively vulnerable, resilient or neutral forest associated with each (left axis) and the mean relative resilience (blue horizontal lines, right axis), ordered from most vulnerable to most resilient.

in which ecotope factors promote brown-down) across the Amazon basin (Fig. 5a), including the ecotope factor combinations that are conducive (or not) to resilience (Fig. 5b,c).

This functional biogeography reveals the importance of ecotopes in structuring forest drought response: first, simply because the GAM models that accounted for forest ecotopes (through the variables HAND, SoilFertility, SoilTexture and ForestHeight; Extended Data Fig. 2) along with climate had significantly more predictive power (higher R^2 while selected by lower Akaike information criterion (AIC)) than climate-only models (Supplementary Table 1). Importantly, the ecotope-defined biogeography allows attribution of greening-inferred resilience in different forests to distinct mechanisms. For example, during the 2015/2016 drought, forest greening was observed both in the shallow-water-table forests of the Rio Negro basin and in deep-water-table forests of Amapa state (RN and AP regions, respectively, highlighted in Figs. 1c, 4b and 5a). The biogeography (Fig. 5b) and GAM prediction (Fig. 4b) show both regions sharing infertile soils, but they point in particular to forest height—and associated deep rooting zones enabling access to deep water—as a key factor supporting resilience/greening in the deep-water-table forests of AP (Fig. 5b,c (orange)), whereas the RN forests (Fig. 5b,c (green)), although short, had access to shallow water tables.

This analysis goes beyond previous climate-based explanations of Amazon forest drought response and, importantly, complements a recent map of external anthropogenic tipping-point threats (due to combined stresses of droughts, deforestation, fire, roads and so on)[6] with a biogeography of intrinsic ecological resilience/vulnerability (due to characteristics of forests in their adapted environments). Interaction among the three different hypotheses—that hydrological environments, soil fertility and tree drought resistance traits structure forest drought response—shows that no single factor could explain drought response across the whole basin through different droughts. Thus, shallow-water-table hydrological environments do indeed protect against drought[24], but only relatively, especially in regions in which high fertility stimulates the fast growth of hydraulically more vulnerable trees[28] (see Fig. 5c, in which the blue-labelled fertile regions with shallow water tables are the least vulnerable among the first four 'more vulnerable' combinations on the left). The most resilient forest types (Fig. 5c) were those with low soil fertility, occupying all categories of the 'more resilient' end of the drought-response biogeography (Fig. 5c (right)).

Confidence in this forest biogeography arises from corroboration by ground observations, and by consistent results from different modelling approaches (in which structural causal models (Extended Data Fig. 6) confirm that GAM predictive models (Figs. 3 and 4) reflect causal effects). Remote-sensing observations generally align well with ecosystem photosynthetic fluxes derived from towers on the ground (see Methods, 'Remote sensing validation and consistency'). Here, they also align with tree demography during the three droughts (Fig. 3a versus Fig. 3d for 2005 and 2010, and Extended Data Fig. 9c–h for 2015) and with remote photosynthetic anomalies, which are negatively correlated with mortality and positively with recruitment, as expected if more-negative anomalies are associated with increased plant stress. Notably, our GAM-derived remote-sensing resilience map also independently predicted observations in forest plots of tree xylem hydraulic safety margins (HSMs) to mortality-inducing embolism[50], a widely cited physiological drought-tolerance trait (Fig. 5a (inset)).

Implications of a functional biogeography

This study has important implications for understanding forest responses to climatic variability and change. First, because shallow-water-table forests in Amazonia are extensive (30–40% of the southern Amazon, where they are found to be protective during drought) but neglected by most previous studies of forest drought sensitivity (Fig. 3e), southern Amazon forests are probably more resilient to drought than common estimates of climate sensitivity imply[16], and large-scale plot-based estimates of a drought-induced decline in the Amazon forest carbon sink[2] may need to be adjusted to account for these higher-drought-resilience but neglected forests.

However, this analysis also warns that climate change is probably simultaneously undermining different strategies and capacities for drought resilience, and highlights specific mechanisms and Amazon regions that are likely to be vulnerable to tipping-point failure: the resilience conveyed by shallow-water-table hydrological environments in certain regions[28] is probably limited under growing climate change. The buffering effect of shallow water tables appears limited

to short-duration droughts (< 3 months; Fig. 3c) that do not last long enough to deplete water tables. The benefits of regrowing trees quickly that are lost to once-in-a-century droughts[28] (whether or not protected by shallow water tables) are much reduced when those drought frequencies increase to become 5 or 10-year droughts (as seen recently and as predicted to continue in the near future[51,52]). Importantly, these fertility results imply (consistent with a recent ground-based study of hydraulic traits[29]) that it is Amazonia's most productive higher-fertility forests that are most vulnerable to future climate change.

Finally, we note that the geographical distribution of these most-vulnerable forests (Fig. 5a (reddish regions)) has important warnings for sustaining the integrity of critical ecosystems both in the basin and beyond. First, these vulnerable forests are at high risk of deforestation (substantially overlapping with the 'arc of deforestation'; Extended Data Fig. 10d). Importantly, because they are predominantly situated under prevailing winds that bring moist Amazonian air to the south (Extended Data Fig. 10d), they are critical to maintaining the evapotranspiration that feeds (and probably amplifies[53]) the 'atmospheric rivers' that bring forest-recycled precipitable water from the Amazon regions to sustain South America's breadbasket in the agricultural regions of Brazil[54].

This unified understanding of the functional biogeography of Amazon drought response provides a basis both for establishing basin-wide priorities for conservation planning[8] and for achieving improved understanding and predictions of tropical forest vulnerability to current droughts, threatened tipping points and future climate change.

Online content

Any methods, additional references, Nature Portfolio reporting summaries, source data, extended data, supplementary information, acknowledgements, peer review information; details of author contributions and competing interests; and statements of data and code availability are available at https://doi.org/10.1038/s41586-024-07568-w.

1. Pan, Y. et al. A large and persistent carbon sink in the world's forests. *Science* **333**, 988–993 (2011).
2. Brienen, R. J. W. et al. Long-term decline of the Amazon carbon sink. *Nature* **519**, 344–348 (2015).
3. Wigneron, J.-P. et al. Tropical forests did not recover from the strong 2015–2016 El Niño event. *Sci. Adv.* **6**, eaay4603 (2020).
4. Gatti, L. V. et al. Amazonia as a carbon source linked to deforestation and climate change. *Nature* **595**, 388–393 (2021).
5. Boulton, C. A., Lenton, T. M. & Boers, N. Pronounced loss of Amazon rainforest resilience since the early 2000s. *Nat. Clim. Chang.* **12**, 271–278 (2022).
6. Flores, B. M. et al. Critical transitions in the Amazon forest system. *Nature* **626**, 555–564 (2024).
7. Oyama, M. D. & Nobre, C. A. A new climate-vegetation equilibrium state for Tropical South America. *Geophys. Res. Lett.* **30**, 2199 (2003).
8. Science Panel for the Amazon. *Amazon Assessment Report 2021* (UN SDSN, 2021).
9. Saleska, S. R., Didan, K., Huete, A. R. & da Rocha, H. R. Amazon forests green-up during 2005 drought. *Science* **318**, 612 (2007).
10. Brando, P. M. et al. Seasonal and interannual variability of climate and vegetation indices across the Amazon. *Proc. Natl Acad. Sci. USA* **107**, 14685–14690 (2010).
11. Xu, L. et al. Widespread decline in greenness of Amazonian vegetation due to the 2010 drought. *Geophys. Res. Lett.* https://doi.org/10.1029/2011gl046824 (2011).
12. Yang, J. et al. Amazon drought and forest response: largely reduced forest photosynthesis but slightly increased canopy greenness during the extreme drought of 2015/2016. *Glob. Change Biol.* **24**, 1919–1934 (2018).
13. Anderson, L. O. et al. Vulnerability of Amazonian forests to repeated droughts. *Philos. Trans. R. Soc. Lond. B* **373**, 20170411 (2018).
14. Anderegg, W. R. L., Trugman, A. T., Badgley, G., Konings, A. G. & Shaw, J. Divergent forest sensitivity to repeated extreme droughts. *Nat. Clim. Change* **10**, 1091–1095 (2020).
15. Feldpausch, T. R. et al. Amazon forest response to repeated droughts. *Glob. Biogeochem. Cycles* **30**, 964–982 (2016).
16. Phillips, O. L. et al. Drought sensitivity of the Amazon rainforest. *Science* **323**, 1344–1347 (2009).
17. Esquivel-Muelbert, A. et al. Tree mode of death and mortality risk factors across Amazon forests. *Nat. Commun.* **11**, 5515 (2020).
18. Tansley, A. G. The use and abuse of vegetational concepts and terms. *Ecology* **16**, 284–307 (1935).
19. Whittaker, R. H., Levin, S. A. & Root, R. B. Niche, habitat, and ecotope. *Am. Nat.* **107**, 321–338 (1973).
20. Jiménez-Muñoz, J. C. et al. Record-breaking warming and extreme drought in the Amazon rainforest during the course of El Niño 2015–2016. *Sci. Rep.* **6**, 33130 (2016).
21. Marengo, J. A. & Espinoza, J. C. Extreme seasonal droughts and floods in Amazonia: causes, trends and impacts. *Int. J. Climatol.* **36**, 1033–1050 (2016).
22. Longo, M. et al. Ecosystem heterogeneity and diversity mitigate Amazon forest resilience to frequent extreme droughts. *N. Phytol.* **219**, 914–931 (2018).
23. Violle, C., Reich, P. B., Pacala, S. W., Enquist, B. J. & Kattge, J. The emergence and promise of functional biogeography. *Proc. Natl Acad. Sci. USA* **111**, 13690–13696 (2014).
24. Costa, F. R. C., Schietti, J., Stark, S. C. & Smith, M. N. The other side of tropical forest drought: do shallow water table regions of Amazonia act as large-scale hydrological refugia from drought?. *N. Phytol.* **237**, 714–733 (2022).
25. Nobre, A. D. et al. Height above the nearest drainage—a hydrologically relevant new terrain model. *J. Hydrol.* **404**, 13–29 (2011).
26. Sousa, T. R. et al. Palms and trees resist extreme drought in Amazon forests with shallow water tables. *J. Ecol.* **108**, 2070–2082 (2020).
27. Esteban, E. J. L., Castilho, C. V., Melgaço, K. L. & Costa, F. R. C. The other side of droughts: wet extremes and topography as buffers of drought negative effects in an Amazonian forest. *N. Phytol.* **229**, 1995–2006 (2020).
28. Oliveira, R. S. et al. Linking plant hydraulics and the fast-slow continuum to understand resilience to drought in tropical ecosystems. *N. Phytol.* **230**, 904–923 (2021).
29. Garcia, M. N., Domingues, T. F., Oliveira, R. S. & Costa, F. R. C. The biogeography of embolism resistance across resource gradients in the Amazon. *Glob. Ecol. Biogeogr.* **32**, 2199–2211 (2023).
30. Chitra-Tarak, R. et al. Hydraulically-vulnerable trees survive on deep-water access during droughts in a tropical forest. *N. Phytol.* **231**, 1798–1813 (2021).
31. Brum, M. et al. Hydrological niche segregation defines forest structure and drought tolerance strategies in a seasonal Amazon forest. *J. Ecol.* **107**, 318–333 (2019).
32. Tumber-Dávila, S. J., Schenk, H. J., Du, E. & Jackson, R. B. Plant sizes and shapes above and belowground and their interactions with climate. *N. Phytol.* **235**, 1032–1056 (2022).
33. Giardina, F. et al. Tall Amazonian forests are less sensitive to precipitation variability. *Nat. Geosci.* **11**, 405–409 (2018).
34. ter Steege, H. et al. Continental-scale patterns of canopy tree composition and function across Amazonia. *Nature* **443**, 444–447 (2006).
35. McDowell, N. et al. Mechanisms of plant survival and mortality during drought: why do some plants survive while others succumb to drought? *N. Phytol.* **178**, 719–739 (2008).
36. Anderegg, W. R. L. et al. Meta-analysis reveals that hydraulic traits explain cross-species patterns of drought-induced tree mortality across the globe. *Proc. Natl Acad. Sci. USA* **113**, 5024–5029 (2016).
37. Lyapustin, A. I. et al. Multi-angle implementation of atmospheric correction for MODIS (MAIAC): 3. Atmospheric correction. *Remote Sens. Environ.* **127**, 385–393 (2012).
38. Li, X. & Xiao, J. A Global, 0.05-degree product of solar-induced chlorophyll fluorescence derived from OCO-2, MODIS, and reanalysis data. *Remote Sens.* **11**, 517 (2019).
39. Aragão, L. E. O. C. et al. Spatial patterns and fire response of recent Amazonian droughts. *Geophys. Res. Lett.* https://doi.org/10.1029/2006gl028946 (2007).
40. Hastie, T. J. & Tibshirani, R. J. *Generalized Additive Models* (CRC, 1990).
41. Pearl, J. Causal inference in statistics: an overview. *Statist. Surv.* **3**, 96–146 (2009).
42. Aragão, L. E. O. C. et al. 21st Century drought-related fires counteract the decline of Amazon deforestation carbon emissions. *Nat. Commun.* **9**, 536 (2018).
43. Zuquim, G. et al. Making the most of scarce data: mapping soil gradients in data-poor areas using species occurrence records. *Methods Ecol. Evol.* **10**, 788–801 (2019).
44. Hengl, T. et al. SoilGrids250m: global gridded soil information based on machine learning. *PLoS ONE* **12**, e0169748 (2017).
45. Simard, M., Pinto, N., Fisher, J. B. & Baccini, A. Mapping forest canopy height globally with spaceborne lidar. *J. Geophys. Res.* https://doi.org/10.1029/2011jg001708 (2011).
46. Christina, M. et al. Almost symmetrical vertical growth rates above and below ground in one of the world's most productive forests. *Ecosphere* **2**, 1–10 (2011).
47. da Costa, A. C. L. et al. Effect of 7 yr of experimental drought on vegetation dynamics and biomass storage of an eastern Amazonian rainforest. *N. Phytol.* **187**, 579–591 (2010).
48. Nepstad, D. C., Tohver, I. M., Ray, D., Moutinho, P. & Cardinot, G. Mortality of large trees and lianas following experimental drought in an Amazon forest. *Ecology* **88**, 2259–2269 (2007).
49. Phillips, O. L. et al. Drought–mortality relationships for tropical forests. *N. Phytol.* **187**, 631–646 (2010).
50. Tavares, J. V. et al. Basin-wide variation in tree hydraulic safety margins predicts the carbon balance of Amazon forests. *Nature* **617**, 111–117 (2023).
51. Duffy, P. B., Brando, P., Asner, G. P. & Field, C. B. Projections of future meteorological drought and wet periods in the Amazon. *Proc. Natl Acad. Sci. USA* **112**, 13172–13177 (2015).
52. Wunderling, N. et al. Recurrent droughts increase risk of cascading tipping events by outpacing adaptive capacities in the Amazon rainforest. *Proc. Natl Acad. Sci. USA* **119**, e2120777119 (2022).
53. Makarieva, A. M. et al. The role of ecosystem transpiration in creating alternate moisture regimes by influencing atmospheric moisture convergence. *Glob. Chang. Biol.* **29**, 2536–2556 (2023).
54. Costa, M. H. et al. in *Amazon Assessment Report 2021* (eds Nobre, C. et al.) Ch. 7 (UN SDSN, 2021).

Methods

In this study, we applied a hypothesis-testing framework[55,56], using remote-sensing methods to test a sequence of three key ecological hypotheses that predict how different forest types respond to drought. To conduct these tests, we assembled key datasets, including two classic satellite products of vegetation photosynthetic function (the most recent version of the EVI and solar induced fluorescence (SIF) (including their validation), gridded products of climate, water-table depth, soil fertility and texture, and vegetation properties defining ecotopes. We focused on intact evergreen forests, mapping data in areas corresponding to evergreen forest cover in non-floodplain, non-deforested forest regions. We assembled field datasets of forest demography (from RAINFOR[2] and ref. 26) and of physiological drought tolerance[50] to test remote sensing skill at capturing ground-measured metrics for forest drought response.

To conduct the statistical analysis, we first interpolated data products onto grids of appropriate spatial resolution, and conducted a supervised classification analysis of Amazon forests into three distinct regions defined by ecotope. We defined climate anomalies and drought characteristics and duration on a pixel-by-pixel basis, defined forest drought resilience in terms of anomalies in vegetation function, conducted a variogram analysis to remove effects of spatial autocorrelation, and then evaluated the scale dependence or sensitivity of key results to the pixel size/spatial resolution. We derived statistical models of drought response using two independent approaches: predictive regression modelling (GAM, a nonlinear multiple regression technique whereby the most predictive models are selected by an information criterion), and SCM (using directed acyclic graphs (DAG)). We tested GAM predictions by comparison to adjusted observations and then used the basin-wide GAM predictive model to derive a functional biogeography of drought response.

Finally, we addressed confidence in our interpretations by exploring potential alternative mechanisms and caveats, and by using the predictive GAM framework to conduct tests of alternative hypotheses that could either support or reject those presented in the main text. These provided evidence in support of our interpretation, but also pointed to future research needs.

Datasets

Remote-sensing indices of photosynthesis. We applied two widely used, ground-validated remote-sensing indices of photosynthesis to provide a sensitivity analysis that brackets the plausible range of forest canopy response to drought: the EVI, constructed from observations of surface reflectance by the MODerate resolution Imaging Spectroradiometer (MODIS) onboard the Terra/Aqua satellites; and the GOSIF product derived from observations by the Orbiting Carbon Observatory 2 satellite. EVI, derived from the spectra of light reflected from surface vegetation, is designed as an index of the photosynthetic capacity[57]. GOSIF is designed to represent the active light emission from fluorescing chlorophyll molecules during photosynthesis, which is often well-correlated with canopy-scale instantaneous photosynthetic activity[57]. This distinction (between reflected light used to construct EVI as a proxy for capacity, versus actively emitted light used to construct GOSIF as a proxy for activity) means that these indices may be expected to display divergent responses.

We chose these indices because they aim to capture different end-members of a spectrum of canopy responses: from transient physiological changes in photosynthesizing/fluorescing leaves (which might be due, for example, to stomatal regulation in response to changing atmospheric VPD) that affect photosynthetic activity for a given capacity[58], versus more structural responses associated with leaf turnover such as leaf flushing or shedding which also change canopy photosynthetic capacity[59]. We primarily focus here on EVI responses, which have been shown to remotely capture seasonal canopy green-up dynamics that are consistent with underlying mechanisms of leaf development and demography[60]. However, GOSIF corroboration of EVI drought responses at broadscales would suggest that ecophysiological and structural canopy responses to drought are aligned in the Amazon, increasing confidence in the robustness of remotely observed drought responses.

MAIAC EVI. The MAIAC algorithm rigorously accounts for sun-sensor geometry, as represented in a bidirectional reflectance distribution function (BRDF), estimating reflectance at a nadir view and 45° solar zenith angle, with strict atmosphere, aerosol and cloud corrections[37]. We used the 8 day MCD19A3 (MAIAC) 1 km product from MODIS collection six, a level 3 product composited from cloud-free and low-aerosol conditions. We applied the coefficients (weights) of the RossThick/Li-Sparse BRDF model (available online https://e4ftl01.cr.usgs.gov/MOTA/MCD19A3.006/). We calculated the 8 day EVI from the MAIAC surface reflectances of red, blue and near-infrared bands as previously[57] from 2001 to 2019. The 8 day EVI is then aggregated to a monthly time step.

GOSIF. SIF, emitted by chlorophyll molecules in green plants that have been excited by absorption of sunlight, provides a direct index of the current physiological state of a photosynthesizing canopy[61]. The OCO-2 satellite observes SIF at coarse resolutions[62], and these are used to create the modelled GOSIF data product[38] (available at http://data.globalecology.unh.edu/data/GOSIF_v2), which simulates higher-resolution SIF dynamics over longer time periods by interpolating among discrete OCO-2 SIF soundings using the MODIS surface reflectance product MCD43C4 (BRDF-corrected to nadir view and to the solar zenith angle at local noon), and meteorological reanalysis data[38]. We used the monthly composite GOSIF product with high spatial resolution of 0.05° over the period from 2001 to 2019. Among SIF-related products, GOSIF has been found to be the best predictor of gross primary productivity (GPP) measured from eddy covariance towers across land cover types[63].

Climate variables

To explore climate effects on forest drought responses, we used monthly precipitation, MCWD, surface downwelling shortwave radiation and VPD resampled at 0.4°. Precipitation and MCWD are from the Global Precipitation Mission and Tropical Rainfall Measuring Mission 3B43-v7 for 2000–2020 at 0.25° resolution (~25 km × 25 km) (https://disc2.gesdisc.eosdis.nasa.gov/data/TRMM_L3/TRMM_3B43.7/)[64].

MCWD measures local drought intensity, defined as the maximum deficit reached in the last month of a string of dry months for each grid cell within the year[39], treating forest water deficit as analogous to a bucket of which the deficit is zero when the bucket is full. To avoid splitting a string of dry months between 2 years, we used a 12-month 'hydrological year' running from May to the following April (for example, MCWD for 2004 was calculated using CWD data from May 2004 to April 2005). We also used monthly surface downwelling shortwave radiation from Modern-Era Retrospective analysis for Research and Applications version 2 (MERRA-2 Reanalysis) for 2000 to 2019 as a proxy for PAR at a spatial resolution of 0.5° × 0.625° (https://goldsmr4.gesdisc.eosdis.nasa.gov/data/MERRA2_MONTHLY/M2TMNXRAD.5.12.4/)[65]. VPD was calculated based on surface air temperature and relative humidity (L3 Standard Monthly Product, AIRS3STM) from version 6 of the Atmospheric Infrared Sounder (AIRS) at a spatial resolution of 1° for 2003–2017 (~100 km; https://airs.jpl.nasa.gov/data/get-data/standard-data/)[66–69].

Ecotope variables

We follow the ecosystem ecology approach[18,19] of characterizing different ecosystem types (in this case, forest ecosystems) by their ecotopes, that is, by the combination of biotic characteristics and abiotic environments that define them, here including their hydrological environment

(water-table depth), soil types (fertility and texture), vegetation characteristics and other factors[70].

We used the HAND-normalized terrain model[25,71] as a proxy of water-table depth and for plant access to groundwater, rederived at 100 m resolution from digital elevation model-Shuttle Radar Topography Mission (SRTM) data for this study[26,72]. The HAND normalization is relative to the local drainage height, using the flow paths to connect all cells (pixels) with the cells of the nearest drainage. The HAND model has been validated over an area of 18,000 km^2 in the lower Rio Negro catchment[25] and used for a wide range of ecohydrological studies[27,73,74]. HAND is comparable to the water-table depth model-based product of a previous study[75], which gave broadly similar results to those reported here with HAND. For this study the HAND-normalized terrain model was derived from SRTM-DEM at a 100 m resolution.

For soil fertility, we used a map (0.1° spatial resolution) of exchangeable base cations (Ca^+ + Mg^+ + K^+ measured in cmol(+) kg^{-1}) for the Amazon basin[43], the most extensive empirically validated gridded soil fertility product currently available. Soil cation concentrations estimated from this product achieved good agreement with an independent dataset of field-measured values (correlation of $r = 0.71$)[43].

Our analysis does not include phosphorus, which is generally considered to be limiting to tropical forest productivity[76,77], but was not available as a high-quality validated gridded data product at the time of our analysis (in the late stages of production of this Article, a phosphorous map for the Amazon was published[78], which we were not able to include in the analysis here). We expect base cations to be a partial index of phosphorus availability, as both cations and phosphorus become available through weathering of young soils arising from Andean parent material or runoff sediment, but are eventually leached, leaving older highly weathered soils in the Guiana Shields depleted of both. Cation concentration should also be directly relevant to drought tolerance, as high concentrations should improve osmotic regulation of stomatal conductance, an important regulator of drought response[79].

For soil texture, we used soil sand/clay fractions from the SoilGrids system released by the International Soil Reference Information Centre World Soil Information[44].

For forest height, we used a canopy height metric derived from spaceborne lidar measurements[45] (https://webmap.ornl.gov/ogc/dataset.jsp?dg_id=10023_1) and validated by field measurements, with an increased accuracy in the Amazon compared to previous metrics[33]). This wall-to-wall global map of canopy height is at a 1 km spatial resolution, interpolated from lidar observations by the Geoscience Laser Altimeter System aboard the Ice, Cloud and Land Elevation Satellite. We take forest canopy height as a proxy of rooting depth, based on standard allometries backed by observations in Brazilian tree plantations[31,32,46], in a central Amazon forest[31,32,46] and across biomes[31,32,46] that show they are correlated[31,32,46]. However, observations of the tree height–rooting depth allometry are limited, especially in tropical forests (although one study cited here[31] is directly relevant, as it is from central-eastern Amazon upland forest, conducted during the 2015 drought); this limitation remains a key uncertainty in our ability to confidently attribute variations in drought response to rooting depth, as opposed to canopy height itself, or other (as yet unidentified) correlates of canopy height. We also note that shallow water-table depth limits rooting depth such that canopy height correlations with rooting depth in these forests may be diminished[80].

We also applied community-weighted mean wood density and the abundance of Fabaceae (legumes)[34]. Fabaceae refers to a large, nearly cosmopolitan family that relates woody plants with nitrogen-fixing nodulation, usually assumed adaptations to low-fertility soils[81].

Identification of terra firme Amazon basin forests using land-cover maps

To focus our analysis on the desired domain of terra firme forests, we used a forest map at 1 km spatial resolution (MCD12Q1.006) to identify evergreen forest pixels within the Amazon basin[82], excluding open water, deforested forests and non-forest vegetation types. A floodplain map was also used to identify targeted non-flooded forests, and exclude floodplain forests[83]. We used the map of a previous study[84] to define the boundary of the Amazon basin, an inclusive definition encompassing all forested parts of the Amazon river catchment and Amazon forests technically within the Orinoco river catchment. We used a recently published forest cover classification that now includes a category for 'degraded' forests at a 30 m spatial resolution[85] (updated to 2022), to test drought sensitivity (see the 'Testing alternative interpretations and considering caveats' section).

Forest plot data

RAINFOR long-term forest plots. We used demographic datasets over the period 1983–2011 from all of the 321 re-censused forest plots that were published and used to estimate Amazon basin-wide carbon balance (most, but not all, of these were from the RAINFOR network)[2], for three purposes: (1) to characterize the spatial representativity of the reported plot-based sampling efforts (area-weighted frequency × duration that plots were monitored) with respect to the distribution of water-table depths (HAND) across the Amazon basin (Fig. 3e); (2) to test whether forest mortality anomalies (percentage deviation from the long-term mean) in 247 plots subject to the 2005 and 2010 droughts were associated with water-table depth (Fig. 3d); and (3) to validate EVI remote sensing with spatial variations in long term (2000–2011) average aboveground net primary productivity (ANPP) rates across the Amazon basin (see the 'Validation by forest plot metrics of demography and of physiological drought tolerance' section; Extended Data Fig. 9a,b). The full RAINFOR and related networks sample more plots than these, likely including a greater range of environments[86], but published results representing drought response of 'the Amazon rainforest'[16] and 'the Amazon carbon sink'[2] are the ones of which the sample plot distributions are analysed here for their representivity.

Shallow water table forest plots. For remote-sensing validation, we also used mortality and recruitment data from 251 ha plots distributed across 8 research sites along the BR-319 road in the southern Amazon between Manaus and Porto Velho (from 62.5° W, 5.9° S to 60.9° W, 4.4° S) as analysed previously[26]. These are shallow-water-table sites (2.81 ± 2.38 m deep (mean ± s.d.)) intended to complement the on average deeper water table sites of the RAINFOR network (above). These more recent data focused on mortality and recruitment rates calculated for the 2015–2016 drought (see the 'Validation by forest plot metrics of demography and of physiological drought tolerance' section; Extended Data Fig. 9c–h).

Forest plot HSMs. We used a pan-Amazon hydraulic trait dataset (HSMs, the difference between water potentials experienced by a species in the field and the water potentials leading to hydraulic failure, with narrower margins indicating greater mortality risk) published by Tavares et al.[50], including 108 species distributed across 9 forest sites across western, central eastern and southern Amazon, to validate our derived resilience map (Fig. 5). These sites belong to old-growth lowland forests, little disturbed by human activities, spanning the Amazonian precipitation gradient and encompassing the principal axes of species composition in the Amazon[50]. The HSM used here was calculated by Tavares et al. as HSM_{50}, the difference between minimum observed stem water potential and P_{50}, the stem water potential at which 50% of xylem hydraulic conductivity is lost. The measurements are conducted on individual trees, then aggregated to the species level; basal-area weighted averages were then calculated for each plot[50].

Remote-sensing validation and consistency

Validation by ecosystem flux measurements (eddy flux towers). MAIAC EVI: EVI has been extensively validated against measurements

of ecosystem photosynthesis (GPP) from eddy flux towers across land types world-wide[87], including temperate[88–90] and tropical[91–93] biomes. Earlier versions of MODIS EVI were criticized as influenced by aerosol or sun-sensor geometry artifacts when detecting tropical forest greening[94,95], but such effects are largely eliminated in the current MAIAC EVI product used here (which corrects artifacts from aerosol contamination and sun-sensor geometry)[37]. Particularly relevant for this study, MAIAC EVI well-detected Amazon forest seasonal green-up dynamics across a network of eddy flux tower sites in the Brazilian Amazon[96,97], with patterns shown to be consistent with understandings of leaf development and demography derived from flux towers and phenocam studies on the ground[60].

EVI or EVI-based models predict independent tower measurements of monthly GPP with R^2 of around 0.5–0.7 for tropical[91–93,96], and R^2 of about 0.7–0.8+ for temperate[88–90] biomes.

GOSIF: despite nonlinear and sometimes decoupled relationships between chlorophyll fluorescence and photosynthesis at leaf scales[98], satellite observations of SIF from OCO-2 have been shown to be linearly related to canopy scale GPP[62], suggesting that canopy-scale processes can effectively average over leafscale complexities. GOSIF-modelled datasets built from SIF observations have been multiply validated by tower-based CO_2 flux estimates of GPP, achieving good correlation (R^2 = 0.73 globally) with the 91 sites of global Fluxnet GPP (2015 tier 1 dataset)[38], with lower correlations (R^2 = 0.51, comparable to EVI in the tropics) for the evergreen broadleaf forest biome, including sites in the Amazon[63].

Note that, for the lower R^2 for tropical versus temperate forest GPP detection, although both indices (GOSIF and EVI) capture GPP comparably in deciduous broadleaf (temperate) versus evergreen broadleaf (tropical) forests within active growing seasons, most statistical assessments are of full annual cycles, which typically show substantially better statistics (R^2 > 0.8) for temperate zone forests, largely because temperate forests include easily detectable dormant periods when GPP ≈ 0, which make total annual variability (hence R^2) higher, while tropical evergreen forests are active year round.

Validation by forest plot metrics of demography and of physiological drought tolerance. We investigated the effect of variations in remotely sensed photosynthesis on downstream forest demographic effects (growth, recruitment and mortality; see the 'Forest plot data' section). We should expect remote-sensing skill in predicting demography to be weaker than for predicting photosynthetic fluxes, because demography emerges not from photosynthesis alone, but from the balance of photosynthesis and autotrophic respiration, and is also influenced by other factors such as disturbance.

We nevertheless found validation at multiple scales: MAIAC EVI significantly predicted spatial variations in decadal forest ANPP (during 2000–2011) across the Amazon basin (RAINFOR network; see the 'Forest plot data' section; Extended Data Fig. 9a,b). Using more recent data, we also confirmed consistent detection by EVI and GOSIF of short-term demographic drought-response metrics during the 2015/2016 drought (mortality, recruitment and the mortality:recruitment ratio; Extended Data Fig. 9c,h), as expected if excess mortality (or a decline in recruitment) follows declines in photosynthetic carbon assimilation. The R^2 values of 0.25 to 0.35 for remote detection of demography (Extended Data Fig. 9) are consistent with our expectation that they should be less than the remote detection R^2 for GPP (0.5 to 0.7, discussed in the 'Validation by ecosystem flux measurements (eddy flux towers)' section), as GPP is only a partial determinant of the NPP driver of demography (NPP = GPP − autotrophic respiration, where autotrophic respiration is not directly detectable by remote sensing, and with perhaps ~60% of the NPP signal due to GPP in the tropics, based on a carbon use efficiency of 0.3 (ref. 99).

With respect to remote detection of the physiological drought tolerance of trees, we investigated the ability of our remote-sensing-derived forest photosynthetic resilience map (Fig. 5a; see the 'Deriving the basin-wide biogeography of forest drought resilience/vulnerability' section) to predict a metric of the resilience of individual trees to drought, HSMs for xylem embolism. Individual tree HSMs—the difference between observed stem water potentials and the stem water potentials at which trees become vulnerable to xylem embolism—are widely regarded as predictors of tree mortality risk under drought[50], with narrower HSMs indicating greater mortality risk[36]. We found that our remote-sensing-derived estimates of forest resilience (Fig. 5a) could significantly predict basal-area weighted tree HSM measured on the ground at forest plots across the Amazon basin (Fig. 5a (inset)) (reported previously[50]; summarized in the 'Forest plot data' section) (note that forest resilience was estimated as described in the 'Deriving the basin-wide biogeography of forest drought resilience/vulnerability' section, but using canopy height mapped at 0.1° resolution, instead of the baseline model resolution of 0.4°, to avoid mixing the height signal of intact HSM plot forests with that of occasionally nearby deforested areas). This comparison strongly supports the validity of using remotely sensed photosynthetic indices to derive a definition of photosynthetic resilience to drought.

Consistency between EVI and GOSIF

Are the two remote sensing metrics showing consistent response to drought? The spatial locations of the drought anomalies appear similar, although not the same (Fig. 1 versus Extended Data Fig. 1d–f) but, as EVI and GOSIF are intended to be sensitive to distinct dimensions of canopy photosynthetic function—that is, to photosynthetic capacity versus activity, respectively (as discussed in the 'Remote sensing indices of photosynthesis' section)—we should not expect sameness.

We do expect activity to be generally more sensitive to drought than capacity, because activity-based responses encompass both transient/reversible physiological responses (for example, stomatal adjustment) as well as slower structural effects due to changes in capacity (for example, biochemical inhibition, leaf growth or shedding)[58,100]. We indeed see this expectation reflected in observed drought response, with the range of GOSIF (activity) anomalies (from −9.6 to +4.8 s.d., excluding 0.1% of the distribution in each tail) 30% greater than the range of EVI anomalies (−6.5 to +4.5 s.d.; insets in Fig. 1 versus Extended Data Fig. 1d–f).

More important, we examine whether there is consistency in terms of support for or rejection of hypotheses that are the focus of this analysis, for example, whether the other-side-of-drought prediction that drought response anomalies should decline with water-table depth, and here we do see broad support for this hypothesis from both EVI and GOSIF: for the 2005 drought 'ellipse' region that was discussed in the main text (Extended Data Fig. 1g), and for the three droughts considered together (Fig. 3a versus Extended Data Fig. 1h). We also see similar ability of the two metrics to predict tree demographic responses to drought on the ground (Extended Data Fig. 9c–h). Together, these comparisons increase confidence that forest drought response hypotheses are robustly supported by the two indices.

Within the broadscale consistency, there are also substantial fine-scale differences in spatial location of anomalies (Fig. 1 versus Extended Data Fig. 1) and the detailed structure of responses (the pattern of residuals in Fig. 3a versus Extended Data Fig. 1h), suggesting that more nuanced study of these finer-scale differences could reveal additional insights into the biogeography of forest drought response[101].

Mapping and statistical analysis

Spatial grid resolutions. We interpolated the differently resolved data products to different grid resolutions as needed for mapping and modelling. Native resolutions were used to display most maps (exceptions noted):

- 1 km for MAIAC EVI (Figs. 1 and 2 and Extended Data Figs. 8b and 9a–e)
- 100 m for HAND, composited to 1 km for mapping (Fig. 2a and Extended Data Fig. 2a)

- 0.05° for GOSIF (Extended Data Figs. 1d–h and 9f–h)
- 0.25° for precipitation-derived products (Extended Data Figs. 2f,g and 3)
- 0.625 × 0.5° for PAR
- 1° for VPD (Extended Data Fig. 3)
- 0.1° for soil fertility (Extended Data Fig. 2b)
- 0.25 km for soil sand content (Extended Data Fig. 2d)
- 1 km for forest canopy height (Extended Data Fig. 2c)
- 1° for wood density and proportion of Fabaceae (Extended Data Fig. 2e,h)

For plotting maps, we used ArcGIS v.10.6.1. For graphing and analysis we used R v.4.2.0 (including R packages ggplot2 for graphics, and FactoMineR, Mgcv and Dagitty for statistical analysis).

For statistical modelling, we interpolated different datasets to common grid resolutions, according to the resolution of the model. For this, we initially downscaled all maps to the native resolution of the EVI product (1 km), then aggregated to the desired coarser resolution, typically 0.4°, that was needed to avoid inflation of statistical significance of drought responses in models by accounting for spatial autocorrelation among nearby pixels using variogram analysis (see the 'Variogram analysis for removal of spatial autocorrelation' section; Supplementary Fig. 1). Grid cells in the drought-affected domain that included no intact forest were excluded from the analysis. When an analysed grid cell (at a coarse resolution, typically 0.4°) included a mix of intact forests and non-forest or deforested regions, we selected and aggregated all intact forest pixels at the smaller (1 km) subgrid scale to accurately represent intact vegetation properties (EVI, canopy height and so on), and represented the coarser model grid cell by those intact forest properties.

Classification of forest regions according to ecotopes. We investigated whether the distribution of factors defining forest types (ecotopes) across Amazonia could lead to a coherent clustering of different forest ecotopes into different regions, each with different broadscale forest drought responses. To this end, we conducted a supervised forest classification, using factors that were identified in previous studies to be important[17,34,102,103]: two climate variables (average minimum monthly precipitation and MCWD variability), soil fertility (concentration of exchangeable base cations[43]) and three tree functional characteristics (forest height, wood density and the proportion of trees in the family Fabaceae).

We conducted the classification in four steps: first, the six ecotope factors, standardized by their mean and s.d., were mapped, with each grid cell considered to occupy a point in a six-dimensional space, and each dimension indexed in comparable units of standard deviations. Second, a principal component analysis (PCA)[104] (FactoMineR package in R; Extended Data Fig. 4a) identified three complementary dimensions of forests in this space: a dimension defined by vegetation characteristics (wood density and proportions of the family Fabaceae), nearly coincident with the first principal component (Extended Data Fig. 4a (x axis)); a dimension defined by water availability (minimum monthly precipitation and MCWD variability), nearly coincident with the second principal component (Extended Data Fig. 4a (y axis)), and a third dimension defined mainly by soil fertility (Extended Data Fig. 4a). On the basis of these initial PCA results suggesting three relatively distinct dimensions, we chose to cluster Amazon basin pixels into three classes. Given their diversity, Amazon forests could probably be classified into more than three, but we judged that three would be sufficient to capture substantial functional variation, without being so complex as to prevent intuitive understanding.

Third, an automatic procedure extracted end-member characteristics based on percentile thresholds[105] from the PCA space[106]. Pixels with low climate variability had high minimum precipitation and long wet seasons (in the 90th percentile), and were identified as a water-availability-spectrum end-member. Grid cells with the highest proportion of Fabaceae, overlaying with tall, dense-wooded trees (in the 90th percentile) and low-fertility soils, were identified as another end-member. A third end-member was defined by a combination of high variability climates and moderately high (67th percentile) soil fertility. Finally, supervised classification using the minimum distance method was used in ENVI (v.5.3)[107] to cluster each region on the basis of the proximity to the end-members selected in step three.

This process identified three clusters of pixels in functional PCA space that turned out to also correspond to geographically distinct Amazonian regions that were mostly contiguous (Extended Data Fig. 4b): an everwet Amazon region in the northwest, a Guiana Shield region in the northeast and the southern Amazon. The standardized values within each cluster of each of the characteristics defining the regional clustering (ordered by water availability, soil fertility and tree traits) exhibit the distinct niches of each region (Extended Data Fig. 4c). The everwet Amazon is differentiated by lack of dry seasons (periods with months with <100 mm rainfall; Extended Data Fig. 2a). Forests in this region might be composed of species that do not well-tolerate climate conditions (such as droughts), compared with tree assemblies (in other regions) adapted to regular droughts or dry seasons. The Guiana Shield region is distinct in having old, highly weathered, low-fertility soils, with tree communities containing the largest proportion of trees in the family Fabaceae, with dense wood and high seed mass[34] (Extended Data Fig. 2c–e). The southern Amazon is then differentiated further from the Guiana Shield as slightly drier, with soil fertility that was both higher on average but also more variable.

This three-region classification (which we use to define the regions depicted in the main text figures) is independent of the results (Figs. 3 and 4) of the basin-wide modelling investigation (described in the 'Statistical analyses for inferring causes of, and predicting, drought response' and 'Comparing adjusted observations to GAM predictions for different predictor variables' sections below) because model predictions depend on pixel-by-pixel variations of environmental factors regardless of what region they are in. However, the three-region Amazon is useful for presenting model results because it illustrates how different functional responses emerge from different ecotope regions (as shown in Fig. 4e).

Climate anomalies for drought definition and mapping. The spatial extent for each of the three droughts (d) was taken to be all grid cells where the MCWD anomaly was more than 1 s.d. below the long-term mean for that cell (Extended Data Fig. 1a–c). MCWD anomaly for each grid cell is calculated by equation (1):

$$\mathrm{MCWD}_{\mathrm{anomaly}} = \frac{\mathrm{MCWD}_d - \overline{\mathrm{MCWD}}}{\sigma_{\mathrm{MCWD}}} \quad (1)$$

where MCWD_d is the data value in drought year (d), $\overline{\mathrm{MCWD}}$ is the average of 19 yearly MCWD values for hydrological years 2000–2019 (May 2000 to April 2020) and σ_{MCWD} is the s.d. for the same time period. Anomalies of the other climate variables were calculated analogously.

Drought severity in each grid cell was classified into three levels by standardized MCWD anomaly: modest drought (−1.5 to −1 s.d. relative to the mean), medium drought (−2 to −1.5 s.d. relative to the mean) and severe drought (greater magnitude than −2 s.d.) (Extended Data Fig. 1a–c).

Drought duration (for each of the three droughts separately for each grid cell) was measured in terms of number of drought months (i) for a particular drought (d) for each grid cell within the period (May to the following April) for the droughts of 2005 and 2010; and from May to October of the following year for the El Nino drought of 2015/2016. The drought onset month is found where the following is true, recalling that CWD and MCWD are more negative with greater water deficit:

$$\begin{aligned} \text{if} \quad & \mathrm{CWD}_{d,i-1} \geq \overline{\mathrm{MCWD}}, \\ & \mathrm{CWD}_{d,i} < \overline{\mathrm{MCWD}}, \\ \text{and} \quad & \mathrm{CWD}_{d,i+1} \leq \overline{\mathrm{MCWD}}, \\ \text{then} \quad & \mathrm{onset}_d = i \end{aligned} \tag{2}$$

The end month of drought interval (i) for each grid cell for each of the three droughts is defined as follows:

$$\begin{aligned} \text{if} \quad & \mathrm{CWD}_{d,j} < \overline{\mathrm{MCWD}}, \\ & \mathrm{CWD}_{d,j+1} \geq \overline{\mathrm{MCWD}}, \\ \text{and} \quad & \mathrm{end}_d \geq \mathrm{onset}_d, \\ \text{then} \quad & \mathrm{end}_d = j \end{aligned} \tag{3}$$

Then for each grid cell, $\mathrm{duration}_d = \mathrm{end}_d - \mathrm{onset}_d + 1$ as shown in Extended Data Fig. 3a–i.

Drought resilience and vegetation anomalies. We defined drought resilience as a forest's ability to increase (or relatively better maintain) photosynthetic capacity or activity during a perturbation—that is, by its tendency to exhibit more positive/less negative anomalies in vegetation indices (relative green-up) during drought. There is a broad literature on resilience[108,109], and our definition (which can also be characterized as 'resistance' or ability to resist changes in function with perturbation[108]) is nominally distinct, for example, from another common definition, the capacity of a system to return to its equilibrium state following a disturbance[110]. We chose relative green-up here for conceptual and practical reasons. Conceptually, greater relative green-up implies relatively more photosynthesis and, therefore, all else equal, more carbon resources to respond to stress, encompassing different strategies (likely including system capacity to return to equilibrium after disturbance), making it a logical general metric of resilience. Practically, greening has been widely cited and discussed in the literature and, notably, is predictive of outcomes on the ground commonly associated with resilience at the individual tree and plot scale (lower mortality, greater growth and greater xylem embolism resistance; see the 'Remote sensing validation and consistency' section; Extended Data Fig. 9c–h).

To quantify photosynthetic resilience, we extracted from each grid cell for each of the three droughts the anomalies in photosynthetic indices for the period of drought (Figs. 1 and 2b,c and Extended Data Figs. 1 and 3), calculated as the departure (in standard deviations from their non-drought-year means) across a 9 year window centred on each drought (for example, 2001–2009 for the 2005 drought and 2011–2019 for the 2015 drought):

$$\mathrm{Anomaly}_{d,\mathrm{du}} = \frac{X_{d,\mathrm{du}} - \overline{X_{\mathrm{du}}}}{\sigma_{\mathrm{du}}}, \tag{4}$$

where $X_{d,\mathrm{du}}$ is the value of the index in a grid cell during drought d, averaged over the duration du (extracted by equations (2) and (3)), and $\overline{X_{\mathrm{du}}}$ and σ_{du} are the average and s.d., respectively, of the same 'du' period across the years of data availability (with the drought years 2005, 2010 and 2015 excluded). Including pixel-specific drought duration introduces greater realism in drought response metrics by capturing pixel–pixel variability in drought response due to duration du, which has been treated in some previous analyses as fixed (for example, in analyses of the 2005 drought, du was assumed to be the 3 months of July, August and September for all pixels)[9,10,111].

Correspondingly, we also calculated the field-based demographic mortality anomalies for drought years 2005 and 2010 from RAINFOR plots[2], as aboveground biomass mortality drought responses (mortality carbon flux after drought, in percentage change relative to long-term mean MgC $\mathrm{ha}^{-1}\,\mathrm{yr}^{-1}$).

Variogram analysis for removal of spatial autocorrelation. Observations from spatial samples are not independent, due to spatial autocorrelation among grid cells that are near to each other[112]. To obtain independent observations for GAMs and for statistical quantification of average drought response (Fig. 1), we resampled grid cells at increasingly coarse resolutions until response differences (between forests with different water-table depths) were no longer spatially autocorrelated—that is, a sill (plateau) was reached in the variogram (Supplementary Fig. 1) at around 40 km, indicating a scale at which the samples could be treated as statistically independent. The variogram was calculated from the covariance of the difference between drought responses in shallow and deep water table grid cells:

$$2\gamma(h) = \frac{1}{N(h)} \sum_{m,n \in N(h)} (z_m - z_n)^2 \tag{5}$$

$$z_m = \mathrm{Anomaly}_{\mathrm{EVI,SWTD}_m} \tag{6}$$

$$z_n = \mathrm{Anomaly}_{\mathrm{EVI,DWTD}_n} \tag{7}$$

where $N(h)$ was the number of grid-cell pairs (m, n) separated by distance h. Each z_m is the standardized EVI anomaly of the first member of a grid cell pair, drawn only from cells with shallow water-table depths (0, 1, 2, …, 9), while z_n is the second member of each pair, drawn only from cells with deep water tables (10, 11, 12, …, 19).

Statistical analyses for inferring causes of, and predicting, drought response. Our statistical analysis had two main goals: first, to test the three core hypotheses presented in the main text introduction (causal inference), and to develop the best possible predictions of regional to basin-wide drought response by combining ecotope factors with climate (predictive inference).

For this, we implemented two sequential statistical approaches: first (see the 'AIC-selected GAMs for hypothesis testing and prediction' section), we used GAM statistical regression[40], selecting among ecologically informed models by the AIC to both test hypotheses about variables thought to influence forest drought response and to identify the best predictive models of regional to basin-wide drought response[113,114]. To avoid known inferential biases of building large regression models out of many variables selected blindly by information criteria like AIC[109,111,112], we construct our moderate-sized models within a hypothesis-testing framework, in which causal hypotheses are specified based on ecological considerations and the selected regression fits test the predictions made by those hypotheses. Second (see the 'SCM using DAG' section), we also used SCM[41,115], an approach that formalizes hypothesis testing as part of the model structure (for example, using DAGs[116,117]). SCM reduces risk from confounding variables that can mask or dilute (or magnify) true causal relationships between the 'exposure' variables (such as climate, soil types) and the 'outcome' variable (such as forest greening/browning)[118]. Note that, in both the GAM and SCM approaches, accurate inference of the relative magnitude or importance of inferred relations is conditional on the model (for example, the diagram in Extended Data Fig. 6) being true.

Finally, we compare the two approaches (see the 'Comparing inferences from SCM with predictive GAM regressions' section) based on the idea that, if the inferences from the two approaches are consistent with each other in terms of their conclusions about hypotheses, this increases the confidence in those conclusions.

AIC-selected GAMs for hypothesis testing and prediction. We developed GAM regression models of forest drought response as a function of climate variables and ecotope factors[10,17,34] to represent our three core hypotheses of water-table depth[24], soil fertility[28,29] and tree characteristics[30–32,50]. GAMs allow for nonlinear relationships between

response and multiple explanatory variables, in which the underlying model structure can be analysed to understand why they make the predictions that they make, in contrast, for example, to machine learning techniques, like boosted regression trees or neural networks[40,119]. GAM links response variables to explanatory variables with a smoothing function, or a spline, that can take a variety of shapes, which are then added together.

We developed GAMs of two types: (1) regional models—fit within regions—designed to test the other-side-of-drought hypothesis 1, by including hydrological environments (as represented by HAND) in addition to climate variables used in previous climate-only regression models of forest drought response[10]; and (2) basin-wide models designed to test all three of our hypotheses together (including effects of soil fertility and tree characteristics) and, in particular, to understand the opposite sensitivity of forest responses to water tables across different regions (Fig. 3a versus Extended Data Fig. 5).

(1) For the effect of local hydrological environment and climate on drought response (regional GAMs), GAMs were fit separately for the southern Amazon, Guiana Shield and everwet Amazon regions, and for all three droughts together, as:

$$\Delta\mathrm{EVI} = s(\mathrm{HAND}) + s(\Delta\mathrm{PAR}) + s(\Delta\mathrm{VPD}) + s(\Delta P) + s(\Delta\mathrm{MCWD}) + s(\mathrm{DL}) + ti(\text{pairwise interactions of every two predictors}) + \varepsilon \quad (8)$$

where ΔEVI is the vegetation response anomaly, ΔPAR, ΔVPD, ΔP and ΔMCWD are the radiation, VPD, precipitation and MCWD anomalies, respectively; DL denotes the drought length; ε is the normally distributed residual; $s()$ and $ti()$ are the smoothing functions of predictor variables, obtained using a scatterplot smoothing algorithm with a back-fitting procedure for the appropriate smoothing function for each predictor. The degree of freedom (d.f.) for the smoothers is determined using the restricted maximum-likelihood (REML) method with Gaussian distribution implemented by the R package mgcv[119]. Models were implemented with the gam.check function of the R package mgcv[119] for diagnostics of residual, distribution and k basis dimension as well as concurvity. All of the predictors were scaled to the same range and unit (40 km or ~0.4°).

The smooth functions were determined by thin plate splines[120,121]. Here, we fitted thin plate regression splines using automatically optimized smoothing parameters using the REML method. Three optimal models were selected for the corresponding three regions, with all three model selection procedures evaluated by delta AIC and R^2 (ref. 113) using the dredge function of the mgcv package in R[119], with results reported in Supplementary Table 1 (models a, b and c).

(2) For the effect of hydrological environment interacting with regional ecotopes (basin-wide GAM), we included soil types (fertility and texture) and vegetation characteristics (forest height, wood density) into the GAM of section (1). Without specifying regions, we aimed to explore whether soil and vegetation characteristics (Extended Data Fig. 2) are able to explain regional differences in the sensitivity of forest response to water-table depth. GAMs were fitted across the whole basin for the 2015/2016 El Niño drought, the only drought that had substantial simultaneous impacts on all three regions of the Amazon basin. The forest responses were comprised of three components: (1) the climate predictor variables (PAR anomaly, VPD anomaly, precipitation anomaly and MCWD anomaly); (2) the ecotope-based environmental predictor variables, in addition to HAND, associated with regional differences: soil fertility, soil texture, forest height and wood density; (3) error terms assumed to be a Gaussian distribution. Specifically, GAMs were fitted as below:

$$\Delta\mathrm{EVI} = s(\mathrm{HAND}) + s(\mathrm{SF}) + s(\mathrm{ST}) + s(\mathrm{FH}) + s(\mathrm{DSL}) + s(\Delta\mathrm{PAR}) + s(\Delta\mathrm{VPD}) + s(\Delta P) + s(\Delta\mathrm{MCWD}) + ti(\text{pairwise interactions of every two climate variables}) + ti(\text{pairwise interactions of HAND with other ecotope – based variables and } \Delta\mathrm{PAR}) + \varepsilon \quad (9)$$

where DSL denotes dry-season length, FH denotes forest height, ST denotes soil texture and SF denotes soil fertility. Considering variable correlations (Supplementary Table 2), we avoided choosing highly correlated variables for the same model (which, for example, excluded wood density when soil fertility was in the model). Considering the complexity of the model and computational cost, the pairwise interactions were included separately among ecotope factors, among climate variables, and between HAND and PAR, but did not traverse interactions among every possible pair of variables. The fitting process was the same as for the regional GAMs of (1): smoother determined with REML as implemented by mgcv[119], and models evaluated by delta AIC and R^2 (ref. 113) coded by the dredge function of the mgcv package in R, with the final results reported in Supplementary Table 1 (model d). The basin-wide modelled forest response for the 2015/2016 drought is presented in Extended Data Fig. 10a–c, in which the GAM well-predicts the pattern of response (Extended Data Fig. 10b), but underestimates the extremes of the responses (as evident from residuals in Extended Data Fig. 10c, showing greening/browning patterns beyond the predictions).

Beyond the three more recent hypotheses discussed in the main text, soil texture was also expected to affect soil hydraulic properties and forest ecosystem response to drought[102,122]. We found that forests on sandy soils were more resilient (that is, higher relative green-up) than those on clay soils (which bind water more closely), consistent with the findings of process model studies[22] of clays that bring soils more quickly to wilting points[22]. But again, this depended on water-table depth, and deep-water-table forests also became more vulnerable with increasing sand content (Extended Data Fig. 7a), perhaps because, in the absence of a shallow water resource, sandy soils drained water too quickly.

This final basin-wide GAM model (Supplementary Table 1d) including soil texture (along with water-table depth, forest height and soil fertility) suggests a further hypothesis for how soil texture moderates the effects of forest height and water-table depth on drought response (Extended Data Fig. 7a). The potential counteracting effects of the positively correlated forest height (which increases resilience when water tables are deep) and soil clay fraction (which generally decreases resilience due to binding water more tightly to soil particles) may explain the otherwise puzzling result that the tall forest advantage in deep-water-table forests does not just disappear but reverses in shallow-water-table environments (Fig. 4d). As shown in Extended Data Fig. 7a, the reversal of the general trend (of decreasing resilience as the clay fraction increases, which corresponds to the sand fraction decreasing) in deep-water-table forests (the red lines in Extended Data Fig. 7a reverse as sand content falls below 50%), is associated with increasing forest height, especially in deep-water-table forests. Thus, at the low sand (high clay) end of the spectrum, the effect of soil texture depends strongly on water-table depth: in shallow-water-table depth forests in which tall trees are not advantaged, the negative effect of clay depresses forest drought response but, in deep-water-table depth forests, drought resilience increases again, even with increasing clay (decreasing sand), possibly because the associated taller tree effect outweighs the negative effect of clay soils. This mechanism could serve to improve models of how soil texture modulates drought response[22,123].

SCM using DAG. To further test the causal mechanisms proposed by our three core hypotheses, we used a framework for causal inference from SCM[41,115], DAG analysis[117,124]. We proposed and tested hypothesized causal relationships (represented by DAG diagrams; Extended Data Fig. 6a).

Implementing DAG analysis with the dagitty R package[125], we first developed a DAG diagram for Amazon forest drought response with relevant climate variables and ecotope factors expected from the literature[10,17,34], including our three core hypotheses of water-table depth[24], soil fertility[28,29] and tree characteristics[30–32,50] (Extended Data Fig. 6a). We assessed DAG-data consistency, testing to ensure that unconnected nodes are not correlated, applying root mean square

error of approximation (RMSEA) (R functions localTests and cis.loess to allow potential nonlinear correlations using loess fits[125]; Extended Data Fig. 6b).

We iteratively tested and revised the DAG by repairing detected independence violations between unconnected nodes (that is, where RMSEA was greater than 0.30, as previously[116]), by adding either a new direct causal link between such nodes (after first verifying an ecological basis for the link), or new links to each of the correlated nodes from a common causal node (again, if they made ecological sense). For example, longer DSL should promote generally drier conditions, including greater VPD and MCWD; positive precipitation anomalies will cause higher relative humidity and therefore lower VPD anomaly[33]; higher-clay soils allow taller trees[126], supporting the addition of links between these nodes. These adjustments gave a final DAG with a greater number of links (Extended Data Fig. 6c) and no conditional independence violations among the remaining unconnected nodes (Extended Data Fig. 6d).

Finally, we used the backdoor criterion to test the causal effects of key predictors. For example, Extended Data Fig. 6c illustrates blocking the confounding 'backdoor path' influence of average DSL on the causal relationship between drought length and drought response. Applying this approach, we exposed the influence of each variable of interest on drought response, one-by-one, while blocking (or adjusting for) the influence of backdoor variables on non-causal pathways (that is, pathways in which at least one arrow points in a direction opposite to the hypothesized causal influence)[115,117] (Extended Data Fig. 6e–j). Note that, because the backdoor criterion often yields different sets of control variables for different pairs of causal predictor and outcome of interest[119,120], we separately fit these models to quantify the causal effects of the different predictors of interest.

Comparing inferences from SCM with predictive GAM regressions. We found that both modelling approaches consistently supported the other-side-of-drought hypothesis (hypothesis 1) for forest drought response in the southern Amazon across all three droughts (negative dependence on water-table depth; Fig. 3a and Extended Data Fig. 6e), with associated consistent climate dependencies (positive dependence on sunlight (Fig. 3b and Extended Data Fig. 6f) and declining overall dependence on drought length, but with a peak at ~3 month duration (Fig. 3c and Extended Data Fig. 6g)). Across the basin for the 2015/2016 drought, both modelling approaches supported hypothesis 2, that increasing soil fertility (past a moderate fertility level) would negatively affect drought response (Fig. 4a,c and Extended Data Fig. 6i), and both supported a 'hypothesis 1–hypothesis 3' interaction, finding that increasing forest height (and presumed deeper rooting depth) positively affected drought response in deep-water-table forests, but had the opposite effect in shallow-water-table forests (Fig. 4b,d and Extended Data Fig. 6h). Finally, although not part of the three core hypotheses, both modelling approaches found similar effects of soil texture on drought response (Extended Data Fig. 6j and Extended Data Fig. 7a).

Comparing adjusted observations to GAM predictions for different predictor variables. The observed vegetation indices (MAIAC EVI and GOSIF) were graphed in adjusted form (as climate-adjusted or ecotope-adjusted observations) to compare observed versus predicted relationships with one predictor variable at a time (for example, water-table depth) while adjusting for the effect of the other, potentially influential, predictor variables represented in the GAM models (see the 'AIC-selected GAMs for hypothesis testing and prediction' section above). This is analogous to partial regression plots or adjusted variable plots in conventional regression models[127]. EVI (Figs. 3a and 4e and Extended Data Fig. 5a,b) or GOSIF (Extended Data Fig. 5c,d) observations of anomalies were adjusted by the difference between the full GAM predictions at each pixel and the partial prediction for the median conditions. For example, to plot climate-adjusted EVI/GOSIF versus water-table depth (across different HAND bins) as in Fig. 3a and Extended Data Fig. 5, the adjustment (shown for EVI) was:

$$\begin{aligned}\text{Adjusted}\Delta\text{EVI}_i &= \Delta\text{EVI}_i - \text{Correction}_i \ \text{Correction}_i \\ &= f(\text{HAND}_i,\ \text{Climates}_i) - f(\text{HAND}_i, \overline{\text{Climates}})\end{aligned} \quad (10)$$

where ΔEVI_i is the observed ith EVI anomaly, $f(\text{HAND}_i, \text{Climates}_i)$ is the prediction of the ith EVI anomaly from GAM (model function for equation (8) denoted as $f()$ here) and $f(\text{HAND}_i, \overline{\text{Climates}})$ is the prediction when holding climates constant at the median value of the domain of the prediction (in this case, the median climate within each drought).

Similar calculations are applied to observations in Fig. 4e to account for the regional differences in climates and ecotopes (everwet, Guiana Shield and southern Amazon), while isolating the effects of water-table depth (HAND) on EVI anomalies with the basin-wide GAM model. The correction term applied to equation (9) in the case of Fig. 4e was

$$\begin{aligned}\text{Correction}_i = f(&\text{HAND}_i,\ \text{Climates}_i, \text{SF}_i, \text{ST}_i, \text{FH}_i) \\ &- f(\text{HAND}_i, \overline{\text{Climates}},\ \overline{\text{SF}}, \overline{\text{ST}}, \overline{\text{FH}})\end{aligned} \quad (11)$$

where SF denotes soil fertility, ST denotes soil texture and FH denotes forest height. The domain of the prediction for which median values of ecotope distributions were taken was, in this case, each of the three regions, considered separately.

Deriving the basin-wide biogeography of forest drought resilience/vulnerability. Classic biogeography in ecology focuses on the drivers of the distribution of species and their phylogenies over space and time, as an emergent consequence of their evolutionary histories[128,129]. Here, following recent ideas in the emerging field of functional biogeography[23,130], we extend classic species-based biogeography to derive a functional biogeography of Amazon forest drought resilience and vulnerability. To accomplish this, we used the GAM analysis that included ecotopes and was derived for the whole basin (see the 'AIC-selected GAMs for hypothesis testing and prediction' section; equation (9), Supplementary Table 1d and Extended Data Fig. 10a–c). Resilience (as plotted in Fig. 5a) was defined as the standardized GAM prediction (positive values corresponding to greening and resilience) from the spatially varying ecotope factors alone (with effects of spatial variation in climate removed by setting each pixel's climate factors equal to their basin-wide average during the 2015 drought):

$$\text{Standardized resilience}_i = \frac{\text{Resilience}_i - \overline{\text{Resilience}}}{\text{SD}_{\text{resilience}}} \quad (12)$$

$$\text{Resilience}_i = f(\text{HAND}_i, \text{SF}_i, \text{ST}_i,\ \text{FH}_i, \overline{\text{Climates}}) \quad (13)$$

where Resilience_i is the prediction for pixel i using equation (9) as function $f()$, and $\overline{\text{Resilience}}$ and $\text{SD}_{\text{resilience}}$ denote the mean and s.d. across the basin, respectively.

We defined thresholds conducive to resilience to define ecotope factor groups associated with resilience or vulnerability. Overlapping ecotope factors generally conducive to resilience (shallow water tables, low soil fertility and tall trees) were distributed across the basin (Fig. 5b,c). The resilience thresholds for the different factors were: shallow-water-table forests, <10 m, taken from ref. 25; low soil fertility, exchangeable base cation concentrations $< 10^{-0.35}$ $\text{cmol}^+\ \text{kg}^{-1}$; and tall forests, heights > 32.5 m. The thresholds for soil fertility and forest height were chosen as the level at which the average slope of EVI anomaly sensitivity to HAND changed sign (Fig. 4a,b).

Testing alternative interpretations and considering caveats

To address potential questions about whether alternative interpretations might either undermine or further illuminate our reported results, we identified additional hypotheses posing alternative interpretations.

Among the additional hypotheses we considered were the following five, the first four of which we were able to partially test here with the functional biogeography GAM model:

H1: that spatial scaling artifacts contaminate the results. In particular, it might be that the primary spatial scale of our analysis (~40 km, to achieve statistical independence; see the 'Variogram analysis for removal of spatial autocorrelation' section) is too large and does not reflect the fine scale of individual tree response to drought in distinct environments, raising the question of whether the effects reported here can be confidently attributed to the aggregation of these fine-scale responses, or to some other effect.

To test this hypothesis, we investigated how the sensitivity of forest drought response to water-table depth depended on the scale of the analysis (Extended Data Fig. 8), from 40 km (Fig. 3a, reproduced in Extended Data Fig. 8a) to the native MODIS scale (1 km) (Extended Data Fig. 8b), and across the finer scales (resolved to 30 m using Landsat OLI 8 land surface reflectance; Extended Data Fig. 8c) available for a region near Manaus[131] (at scales below 40 km, spatial autocorrelation is evident; this artificially narrows confidence intervals, but does not hinder the scaling comparisons). These analyses showed that the sensitivity of forest drought response to water-table depth did not detectably depend on scale, adding confidence that the key factor of water-table depth indeed structures Southern Amazon drought response (as in Fig. 3a) across different scales. Note that this analysis suggests a need for future investigation of how the actual magnitudes of greenness anomalies at the ecological neighbourhood scale (1 ha) of operation of community and ecophysiological mechanisms translate to magnitudes at larger scales.

H2: that different aspects of drought dynamics (for example, severity interacting with duration) may confound the reported interpretation of drought duration (Fig. 3). Drought severity and duration are known to have distinct effects on different species in other biomes, raising the question of whether these dimensions of drought have distinct effects in the Amazon.

We tested the interacting effects of severity (as defined as in the 'Climate anomalies for drought definition and mapping' section, by the MCWD anomaly) and drought duration by further analysing the model of Supplementary Table 1a. This analysis (not shown) confirms that droughts that are both deep and long have the most-negative effects on photosynthesis. This also confirmed the hump-shaped response to drought duration reported in Fig. 3c (with a primary hump occurring earlier but persisting longer through a secondary hump for less severe droughts).

H3: that drought impacts during dry seasons are different than during wet seasons, complicating interpretation of PAR anomaly and drought length effects (Fig. 3). If light limitation (and therefore PAR sensitivity) is stronger in the wet season (because light is already more limiting in the wet season due to greater cloud cover), longer droughts will not just be longer, but (because seasons are of finite length) they will also be more likely to encompass, in varying fractions, the differing light sensitivities of dry and wet seasons.

To test whether the proportion of the drought that occurs in the wet versus dry season affects reported forest responses, we constructed DryDrought as a predictor variable, representing the proportion of a given pixel's drought that occurred in the dry season. We, added DryDrought to the GAM for the Southern Amazon (Supplementary Table 1a), comprising HAND, climate factors and the error terms. Specifically:

$$\begin{aligned}\Delta\mathrm{EVI} = {} & s(\mathrm{HAND}) + s(\Delta\mathrm{PAR}) + s(\mathrm{DryDrought}) \\ & + s(\Delta\mathrm{VPD}) + s(\Delta P) + s(\Delta\mathrm{MCWD}) + s(\mathrm{DL}) \\ & + ti(\text{pairwise interactions of every two} \\ & \quad \text{variables except for DryDrought}) \\ & + ti(\mathrm{DryDrought}, \Delta\mathrm{PAR}) + ti(\mathrm{DryDrought}, \mathrm{DL})\end{aligned} \tag{14}$$

This analysis (Extended Data Fig. 7b–d) showed that the longest drought (2015) also had the broadest distribution of occurrences across dry and wet seasons, with about equal parts of the drought occurring in the dry versus the wet season (median fraction in the dry season = 0.51; Extended Data Fig. 7b). By contrast, the 2005 and 2010 droughts were primarily dry-season droughts (median dry-season fractions = 0.83 and 0.77, respectively). This analysis confirms our finding of a generally positive sensitivity of droughted forests to sunlight reported in the main narrative (Fig. 3b), but further shows that the greater the proportion of the drought that occurs in the wet season, the greater the positive sensitivity to sunlight anomalies (in Extended Data Fig. 7c, the blue line representing pixels experiencing predominantly wet-season drought is steeper than the red line representing pixels predominantly experiencing dry-season drought). This analysis also confirms (Extended Data Fig. 7d) that the hump-shaped response to drought duration (as in Fig. 3c, especially the peak of vegetation response at 3 month duration) is general across both dry- and wet-season droughts. A consistent result of both analyses is that (with the exception of PAR anomalies greater than +2 s.d.; Extended Data Fig. 7c), forests experiencing wet-season droughts are generally more negatively affected by drought than are forests experiencing dry-season droughts, consistent with the idea that, although trees are adapted to the dry conditions of annually recurring dry seasons, they are especially vulnerable when droughts hit in the wet (recovery) season.

H4: that deforested or degraded forests may be driving or contaminating results that are reported as for intact forests. Deforested regions are excluded from the analysis, but the mask may still include forests in proximity to deforested regions that, although not deforested, may be experiencing degradation. We conducted a sensitivity test to address the question of whether different drought responses in degraded forests could be contaminating our findings using a recent classification[85] that identifies partially degraded forests as distinct from both deforested and intact forests, now updated through 2022. We repeated the GAM analysis reported in Fig. 4, but excluded pixels representing degraded forests. The results (not shown) were similar to in Fig. 4, but suggested that partially degraded forests are indeed probably more vulnerable. For example, analysis of purely intact (non-degraded) forests gave curves analogous to those in Fig. 4c,d that reached a slightly greater EVI anomaly value than the corresponding curves of Fig. 4c,d (including mainly intact and but also some degraded forests). This suggests that a functional biogeography approach may be fruitful for future investigations of the effect of forest degradation on drought sensitivity at the local scale. However, the differences are slight at the basin scale, and the overall patterns in the results shown in Figs. 4 and 5 do not depend much on whether these forests in between deforested and intact regions are included or excluded.

H5: that relatively taller individual trees are more vulnerable to drought, even as tall-canopy deep-water-table forests are on average more resilient to drought. We found that greater forest canopy height promoted resilience for deep-water-table forests, but increased vulnerability for shallow-water-table forests (Fig. 4d and Extended Data Fig. 6h). Observations of drought responses in the RAINFOR network[49] and drought experiments[47,48], in seeming contrast, report that tall trees were more vulnerable to drought. One of the drought experiments was above a moderately shallow water table (7–10 m) and the vulnerability of tall trees there could be explained by our result[47], but the forest of a previously reported drought experiment[48], and many of the plots in the RAINFOR network, are over deep water tables, raising the question as to whether the results reported here might be inconsistent with those.

Recalling that the satellite-derived canopy heights are not individual tree heights but overall mean heights of forest canopies over a 1 km pixel, we hypothesize that both results are true: that deep-water-table forests that are tall on average (and presumed to have on average deeper roots that bring greater collective access to deep water resources) are more resilient than forests that are on average shorter, but that

individual trees that are relatively taller than their neighbours are subject to greater atmospheric drought stress from higher VPD, and may therefore be individually more vulnerable than their average-height neighbours. Hydraulic redistribution by roots, observed as part of a previous[48] Amazon drought experiment[132] and by other studies, is a mechanism that could further enhance forest benefit from redistributing deep waters upward in the soil profile.

This is a more challenging hypothesis to test and, in contrast to the hypotheses above, it is beyond the scope of our current study to test here. However, this could be tested by extensive plot data or higher-resolution LIDAR data[100,133] that could resolve individual tall trees in the canopy, and compare their drought-induced mortality rates across forests of different average heights.

Reporting summary

Further information on research design is available in the Nature Portfolio Reporting Summary linked to this article.

Data availability

All remote sensing data and products (vegetation/photosynthetic indices (https://lpdaac.usgs.gov/products/mcd19a3v006/, http://data.globalecology.unh.edu/data/GOSIF_v2), climate variables (https://disc2.gesdisc.eosdis.nasa.gov/data/TRMM_L3/TRMM_3B43.7/, https://goldsmr4.gesdisc.eosdisc.nasa.gov/data/MERRA2_MONTHLY/M2TMNXRAD.5.12.4/, https://airs.jpl.nasa.gov/data/get-data/standard-data/), land cover (https://lpdaac.usgs.gov/products/mcd12q1v006/, https://forobs.jrc.ec.europa.eu/TMF), tree characteristics (canopy height, https://webmap.ornl.gov/ogc/dataset.jsp?dg_id=10023_1) and soil texture (https://maps.isric.org/)) are publicly available online. The ground-based demographic validation data are publicly available in refs. 2,26. The ground-based hydraulic trait validation data are publicly available in ref. 50. The HAND data are from ref. 25, which derived them from the digital elevation model from the Shuttle Radar Topography Mission. The soil fertility data are available in ref. 43.

Code availability

Code for reproducing the modelling analysis and figures is posted at Code Ocean (https://codeocean.com/capsule/2432086/tree).

55. Betts, M. G. et al. When are hypotheses useful in ecology and evolution? *Ecol. Evol.* **11**, 5762–5776 (2021).
56. Glass, D. J. & Hall, N. A brief history of the hypothesis. *Cell* **134**, 378–381 (2008).
57. Huete, A. et al. Overview of the radiometric and biophysical performance of the MODIS vegetation indices. *Remote Sens. Environ.* **83**, 195–213 (2002).
58. Santos, V. A. H. F. D. et al. Causes of reduced leaf-level photosynthesis during strong El Niño drought in a Central Amazon forest. *Glob. Change Biol.* **24**, 4266–4279 (2018).
59. Wu, J. et al. Partitioning controls on Amazon forest photosynthesis between environmental and biotic factors at hourly to interannual timescales. *Glob. Change Biol.* **23**, 1240–1257 (2017).
60. Wu, J. et al. Leaf development and demography explain photosynthetic seasonality in Amazon evergreen forests. *Science* **351**, 972–976 (2016).
61. Mohammed, G. H. et al. Remote sensing of solar-induced chlorophyll fluorescence (SIF) in vegetation: 50 years of progress. *Remote Sens. Environ.* **231**, 111177 (2019).
62. Sun, Y. et al. OCO-2 advances photosynthesis observation from space via solar-induced chlorophyll fluorescence. *Science* **358**, eaam5747 (2017).
63. Shekhar, A., Buchmann, N. & Gharun, M. How well do recently reconstructed solar-induced fluorescence datasets model gross primary productivity? *Remote Sens. Environ.* **283**, 113282 (2022).
64. Huffman, G. J., Adler, R. F., Bolvin, D. T. & Nelkin, E. J. in *Satellite Rainfall Applications for Surface Hydrology* (eds Gebremichael, M. & Hossain, F.) 3–22 (Springer, 2010).
65. Gelaro, R. et al. The Modern-Era Retrospective Analysis for Research and Applications, version 2 (MERRA-2). *J. Clim.* **30**, 5419–5454 (2017).
66. Aumann, H. H. Atmospheric infrared sounder on the Earth observing system. *Opt. Eng.* **33**, 776 (1994).
67. Kahn, B. H. et al. The Atmospheric Infrared Sounder version 6 cloud products. *Atmos. Chem. Phys.* **14**, 399–426 (2014).
68. Susskind, J., Blaisdell, J. M. & Iredell, L. Improved methodology for surface and atmospheric soundings, error estimates, and quality control procedures: the atmospheric infrared sounder science team version-6 retrieval algorithm. *J. Appl. Remote Sens.* **8**, 084994 (2014).
69. Sun, J. et al. Global evaluation of terrestrial near-surface air temperature and specific humidity retrievals from the Atmospheric Infrared Sounder (AIRS). *Remote Sens. Environ.* **252**, 112146 (2021).
70. Bastian, O. et al. In *Development and Perspectives of Landscape Ecology* (eds Bastian, O. & Steinhardt, U.) 49–112 (Springer, 2002).
71. Rennó, C. D. et al. HAND, a new terrain descriptor using SRTM-DEM: mapping terra-firme rainforest environments in Amazonia. *Remote Sens. Environ.* **112**, 3469–3481 (2008).
72. Brunner, I., Herzog, C., Dawes, M. A., Arend, M. & Sperisen, C. How tree roots respond to drought. *Front. Plant Sci.* **6**, 547 (2015).
73. Oliveira, R. S. et al. Embolism resistance drives the distribution of Amazonian rainforest tree species along hydro-topographic gradients. *N. Phytol.* **221**, 1457–1465 (2019).
74. Levis, C. et al. Persistent effects of pre-Columbian plant domestication on Amazonian forest composition. *Science* **355**, 925–931 (2017).
75. Fan, Y., Li, H. & Miguez-Macho, G. Global patterns of groundwater table depth. *Science* **339**, 940–943 (2013).
76. Cunha, H. F. V. et al. Direct evidence for phosphorus limitation on Amazon forest productivity. *Nature* **608**, 558–562 (2022).
77. Chadwick, O. A., Derry, L. A., Vitousek, P. M., Huebert, B. J. & Hedin, L. O. Changing sources of nutrients during four million years of ecosystem development. *Nature* **397**, 491–497 (1999).
78. Darela-Filho, J. P. et al. Reference maps of soil phosphorus for the pan-Amazon region. *Earth Syst. Sci. Data* **16**, 715–729 (2024).
79. Liu, H.-Y., Sun, W.-N., Su, W.-A. & Tang, Z.-C. Co-regulation of water channels and potassium channels in rice. *Physiol. Plant.* **128**, 58–69 (2006).
80. Fan, Y., Miguez-Macho, G., Jobbágy, E. G., Jackson, R. B. & Otero-Casal, C. Hydrologic regulation of plant rooting depth. *Proc. Natl Acad. Sci. USA* **114**, 10572–10577 (2017).
81. Hasanuzzaman, M., Araújo, S. & Gill, S. S. *The Plant Family Fabaceae: Biology and Physiological Responses to Environmental Stresses* (Springer, 2021).
82. Friedl, M. A. et al. MODIS Collection 5 global land cover: algorithm refinements and characterization of new datasets. *Remote Sens. Environ.* **114**, 168–182 (2010).
83. Hess, L. L. et al. Wetlands of the lowland Amazon basin: extent, vegetative cover, and dual-season inundated area as mapped with JERS-1 synthetic aperture radar. *Wetlands* **35**, 745–756 (2015).
84. Gómez, J., Schobbenhaus, C. & Montes, N. E. *Geological Map of South America 2019. Scale 1: 5 000 000. Commission for the Geological Map of the World (CGMW), Colombian Geological Survey and Geological Survey of Brazil* (2019); https://doi.org/10.32685/10.143.2019.929.
85. Vancutsem, C. et al. Long-term (1990–2019) monitoring of forest cover changes in the humid tropics. *Sci. Adv.* **7**, eabe1603 (2021).
86. ForestPlots.net, et al. Taking the pulse of Earth's tropical forests using networks of highly distributed plots. *Biol. Conserv.* **260**, 108849 (2021).
87. Shi, H. et al. Assessing the ability of MODIS EVI to estimate terrestrial ecosystem gross primary production of multiple land cover types. *Ecol. Indic.* **72**, 153–164 (2017).
88. Sims, D. A. et al. On the use of MODIS EVI to assess gross primary productivity of North American ecosystems. *J. Geophys. Res.* **111**, G04015 (2006).
89. Rahman, A. F., Sims, D. A., Cordova, V. D. & El-Masri, B. Z. Potential of MODIS EVI and surface temperature for directly estimating per-pixel ecosystem C fluxes. *Geophys. Res. Lett.* **32**, L19404 (2005).
90. Sims, D. A. et al. A new model of gross primary productivity for North American ecosystems based solely on the enhanced vegetation index and land surface temperature from MODIS. *Remote Sens. Environ.* **112**, 1633–1646 (2008).
91. Huete, A. R. et al. Amazon rainforests green-up with sunlight in dry season. *Geophys. Res. Lett.* **33**, L06405 (2006).
92. Huete, A. R. et al. Multiple site tower flux and remote sensing comparisons of tropical forest dynamics in Monsoon Asia. *Agric. For. Meteorol.* **148**, 748–760 (2008).
93. Huete, A. R. Vegetation indices, remote sensing and forest monitoring. *Geogr. compass* **6**, 513–532 (2012).
94. Samanta, A. et al. Amazon forests did not green-up during the 2005 drought. *Geophys. Res. Lett.* **37**, L05401 (2010).
95. Morton, D. C. et al. Amazon forests maintain consistent canopy structure and greenness during the dry season. *Nature* **506**, 221–224 (2014).
96. Saleska, S. R. et al. Dry-season greening of Amazon forests. *Nature* **531**, E4–E5 (2016).
97. Maeda, E. E., Heiskanen, J., Aragão, L. E. O. C. & Rinne, J. Can MODIS EVI monitor ecosystem productivity in the Amazon rainforest? *Geophys. Res. Lett.* **41**, 7176–7183 (2014).
98. Magney, T. S., Barnes, M. L. & Yang, X. On the covariation of chlorophyll fluorescence and photosynthesis across scales. *Geophys. Res. Lett.* **47**, e2020GL091098 (2020).
99. Chambers, J. Q. et al. Respiration from a tropical forest ecosystem: partitioning of sources and low carbon use efficiency. *Ecol. Appl.* **14**, 72–88 (2004).
100. Smith, M. N. et al. Seasonal and drought-related changes in leaf area profiles depend on height and light environment in an Amazon forest. *N. Phytol.* **222**, 1284–1297 (2019).
101. Janssen, T. et al. Drought effects on leaf fall, leaf flushing and stem growth in the Amazon forest: reconciling remote sensing data and field observations. *Biogeosciences* **18**, 4445–4472 (2021).
102. Quesada, C. A. et al. Basin-wide variations in Amazon forest structure and function are mediated by both soils and climate. *Biogeosciences* **9**, 2203–2246 (2012).
103. Lloyd, J. et al. Edaphic, structural and physiological contrasts across Amazon Basin forest–savanna ecotones suggest a role for potassium as a key modulator of tropical woody vegetation structure and function. *Biogeosciences* **12**, 6529–6571 (2015).
104. Wold, S., Esbensen, K. & Geladi, P. Principal component analysis. *Chemometr. Intellig. Lab. Syst.* **2**, 37–52 (1987).
105. Doan, H. T. X. & Foody, G. M. Reducing the impacts of intra-class spectral variability on soft classification and its implications for super-resolution mapping. In *Proc. IEEE International Geoscience and Remote Sensing Symposium* 2585–2588 (IEEE, 2007).
106. Malhi, A. & Gao, R. X. PCA-based feature selection scheme for machine defect classification. *IEEE Trans. Instrum. Meas.* **53**, 1517–1525 (2004).
107. Canty, M. J. *Image Analysis, Classification and Change Detection in Remote Sensing: With Algorithms for ENVI/IDL and Python, Third Edition* (CRC, 2014).

108. Grafton, R. Q. et al. Realizing resilience for decision-making. *Nat. Sustain.* **2**, 907–913 (2019).
109. Nikinmaa, L. et al. Reviewing the use of resilience concepts in forest sciences. *Curr. For. Rep.* **6**, 61–80 (2020).
110. Gunderson, L. H. Ecological resilience—in theory and application. *Annu. Rev. Ecol. Syst.* **31**, 425–439 (2000).
111. Samanta, A. et al. Amazon forests did not green-up during the 2005 drought. *Geophys. Res. Lett.* https://doi.org/10.1029/2009gl042154 (2010).
112. Haining, R. P. & Haining, R. *Spatial Data Analysis: Theory and Practice* (Cambridge Univ. Press, 2003).
113. Burnham, K. P., Anderson, D. R. & Huyvaert, K. P. AIC model selection and multimodel inference in behavioral ecology: some background, observations, and comparisons. *Behav. Ecol. Sociobiol.* **65**, 23–35 (2011).
114. Clark, J. S. *Models for Ecological Data* (Princeton Univ. Press, 2020).
115. Pearl, J. *Causality* (Cambridge Univ. Press, 2009).
116. Ankan, A., Wortel, I. M. N. & Textor, J. Testing graphical causal models using the R package 'dagitty'. *Curr. Protoc.* **1**, e45 (2021).
117. Arif, S. & MacNeil, M. A. Applying the structural causal model framework for observational causal inference in ecology. *Ecol. Monogr.* **93**, e1554 (2023).
118. Arif, S. & MacNeil, M. A. Predictive models aren't for causal inference. *Ecol. Lett.* **25**, 1741–1745 (2022).
119. Wood, S. N. *Generalized Additive Models: An Introduction with R, Second Edition* (CRC, 2017).
120. Quaresma, M., Carpenter, J. & Rachet, B. Flexible Bayesian excess hazard models using low-rank thin plate splines. *Stat. Methods Med. Res.* **29**, 1700–1714 (2020).
121. Schempp, W. & Zeller, K. eds. *Constructive Theory of Functions of Several Variables: Proceedings of a Conference Held at Oberwolfach, April 25 - May 1, 1976* (Springer, 1977).
122. Laurance, W. F. et al. Relationship between soils and Amazon forest biomass: a landscape-scale study. *For. Ecol. Manage.* **118**, 127–138 (1999).
123. Levine, N. M. et al. Ecosystem heterogeneity determines the ecological resilience of the Amazon to climate change. *Proc. Natl Acad. Sci. USA* **113**, 793–797 (2016).
124. Addicott, E. T., Fenichel, E. P., Bradford, M. A., Pinsky, M. L. & Wood, S. A. Toward an improved understanding of causation in the ecological sciences. *Front. Ecol. Environ.* **20**, 474–480 (2022).
125. Textor, J., van der Zander, B., Gilthorpe, M. S., Liskiewicz, M. & Ellison, G. T. Robust causal inference using directed acyclic graphs: the R package 'dagitty'. *Int. J. Epidemiol.* **45**, 1887–1894 (2016).
126. de Castilho, C. V. et al. Variation in aboveground tree live biomass in a central Amazonian Forest: effects of soil and topography. *For. Ecol. Manage.* **234**, 85–96 (2006).
127. Velleman, P. F. & Welsch, R. E. Efficient computing of regression diagnostics. *Am. Stat.* **35**, 234–242 (1981).
128. Webb, C. O., Cannon, C. H. & Davies, S. J. in *Tropical Forest Community Ecology* (eds Carson, W. P. & Schnitzer, S. A.) 79–97 (Wiley–Blackwell, 2008).
129. Humboldt's legacy. *Nat. Ecol. Evol.* **3**, 1265–1266 (2019).
130. Reichstein, M., Bahn, M., Mahecha, M. D., Kattge, J. & Baldocchi, D. D. Linking plant and ecosystem functional biogeography. *Proc. Natl Acad. Sci. USA* **111**, 13697–13702 (2014).
131. Nelson, B. W., Gonçalves, N. B., Chen, S. & Saleska, S. Persistent effect of 2015 El Niño drought on NIR reflectance of central Amazon upland forests? In *Anais do XX Simpósio Brasileiro de Sensoriamento Remoto* 1636–1638 (INPE, 2023).
132. Oliveira, R. S., Dawson, T. E., Burgess, S. S. O. & Nepstad, D. C. Hydraulic redistribution in three Amazonian trees. *Oecologia* **145**, 354–363 (2005).
133. Nunes, M. H. et al. Forest fragmentation impacts the seasonality of Amazonian evergreen canopies. *Nat. Commun.* **13**, 917 (2022).
134. Van der Meer, T., Te Grotenhuis, M. & Pelzer, B. Influential cases in multilevel modeling: a methodological comment. *Am. Sociol. Rev.* **75**, 173–178 (2010).
135. Boers, N., Marwan, N., Barbosa, H. M. J. & Kurths, J. A deforestation-induced tipping point for the South American monsoon system. *Sci. Rep.* **7**, 41489 (2017).

Acknowledgements We thank J. Schietti for early discussions of the idea that remote sensing might be used to investigate the effect of water-table depth on forest drought response; T. R. Sousa for sharing and discussing plot-based forest demographic data (from along the BR-319 road)[26]; G. Zuquim for sharing an early version of mapped basin-wide soil fertility data[43]; H. ter Steege for sharing mapped basin-wide tree characteristics data[34]; T. R. Sousa and J. Schietti for comments on an earlier version of the manuscript; L. Alves for advice on forest demography plots; R. Palacios for recommending the use of GAM models; M. N. Garcia for discussions about soil fertility; N. Boers for advice on the South American monsoon system; T. C. Taylor and V. Ivanov for discussions; J. Cronin and S. McMahon for detailed advice and comments; and S.C.'s doctoral dissertation committee members W. K. Smith, J. Hu and B. Enquist for constructive criticism and advice on the direction of this work. This work was supported by US National Aeronautics and Space Administration, fellowship 80NSSC19K1376 (S.C.); US National Science Foundation, DEB grant 1950080 (S.C.S. and M.N.S.); US National Science Foundation, DEB grant 2015832 (S.R.S.); US National Science Foundation, DEB grant 1754803 (S.R.S., N.R.-C.), US National Science Foundation, DEB grant 1754357 (S.C.S.); Brazil National Council for Scientific and Technological Development (CNPq) scholarships 371626/2022-6, 372734/2021-9,381711/2020-0 (D.d.J.A.); and US Department of Energy's Next Generation Ecosystem Experiments-Tropics (R.C.-T.).

Author contributions S.C. and S.R.S. designed the analysis, based on early conception by A.D.N. and S.R.S., and on funded proposals to investigate 'the other side of tropical forest drought' led by S.C.S., M.N.S. and S.R.S. (from NSF) and by S.C. and S.R.S. (from NASA). A.D.N., L.A.C. and D.d.J.A. updated their HAND data product and interpreted it for this analysis. B.W.N. and N.R.-C. contributed remote-sensing expertise and analysis. R.C.-T. contributed statistical modelling expertise and analysis. H.K. contributed code, especially for the variogram analysis. S.C. organized the datasets (with assistance from N.R.-C.), conducted the analysis and wrote the initial draft. S.C., S.R.S. and S.C.S. revised the draft. All of the authors contributed to writing the final version.

Competing interests The authors declare no competing interests.

Additional information

Supplementary information The online version contains supplementary material available at https://doi.org/10.1038/s41586-024-07568-w.

Correspondence and requests for materials should be addressed to Shuli Chen or Scott R. Saleska.

Peer review information *Nature* thanks Christopher Baraloto, David Bauman, Jovan Tadic and the other, anonymous, reviewer(s) for their contribution to the peer review of this work. Peer reviewer reports are available.

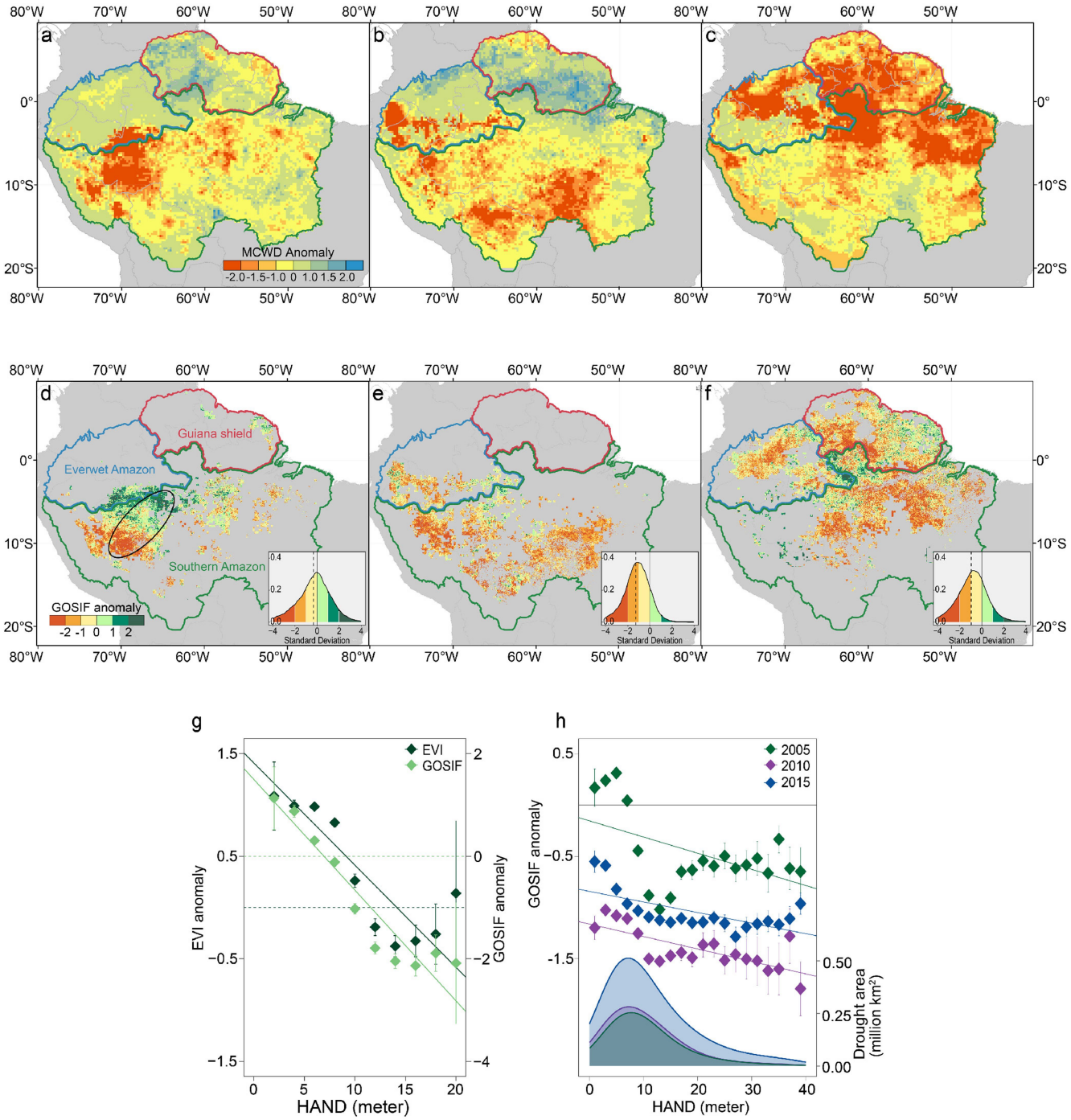

Extended Data Fig. 1 | Drought maps 2005, 2010 and 2015/16 droughts and GOSIF-based forest responses droughts. (a)-(c): Maximum cumulative water deficit (MCWD) standardized anomalies. (relative to the long term mean MCWD across years, blue=positive, orange=negative) during drought for (**a**) 2005, (**b**) 2010, and (**c**) 2015 droughts. MCWD is calculated (see Methods, 'Climate variables') as the maximum water deficit reached for each hydrologic year (from May of the nominal year to the following April). The "drought region" is defined as pixels whose MCWD anomaly is more than one SD below the mean (light orange to red). **(d)-(f): GOSIF-based forest response to droughts.** GOSIF anomalies during drought, relative to the long term mean GOSIF (green=positive, orange=negative) in drought regions for the (**d**) 2005, (**e**) 2010 and (**f**) 2015 droughts, respectively. (**g**) EVI (left axis) and GOSIF (right axis) anomalies in the 2005 drought elliptical region (as depicted in Figs. 1a, 2a, and here in Extended Data Fig. 1d) show consistent patterns versus HAND (bin averages ±95% CI, with N = 6,547 5-km pixels for both EVI and GOSIF); (**h**) GOSIF anomalies (bin averages points ±95% CI and solid regression line) vs. water-table depths (indexed by HAND) support hypothesis 1 (with negative slopes, consistent with EVI in Fig. 3a) for the 2005 (green, slope = −0.016 ± 0.006 SE m^{-1}), 2010 (purple, slope = −0.012 ± 0.003 SE m^{-1}), and 2015 (blue, slope = −0.010 ± 0.003 SE m^{-1}) droughts, paired with HAND distributions in each drought region (bottom graphs, right axis, with N = 34,980, 30,004, 43,475 5-km pixels for 2005, 2010, and 2015 droughts, respectively).

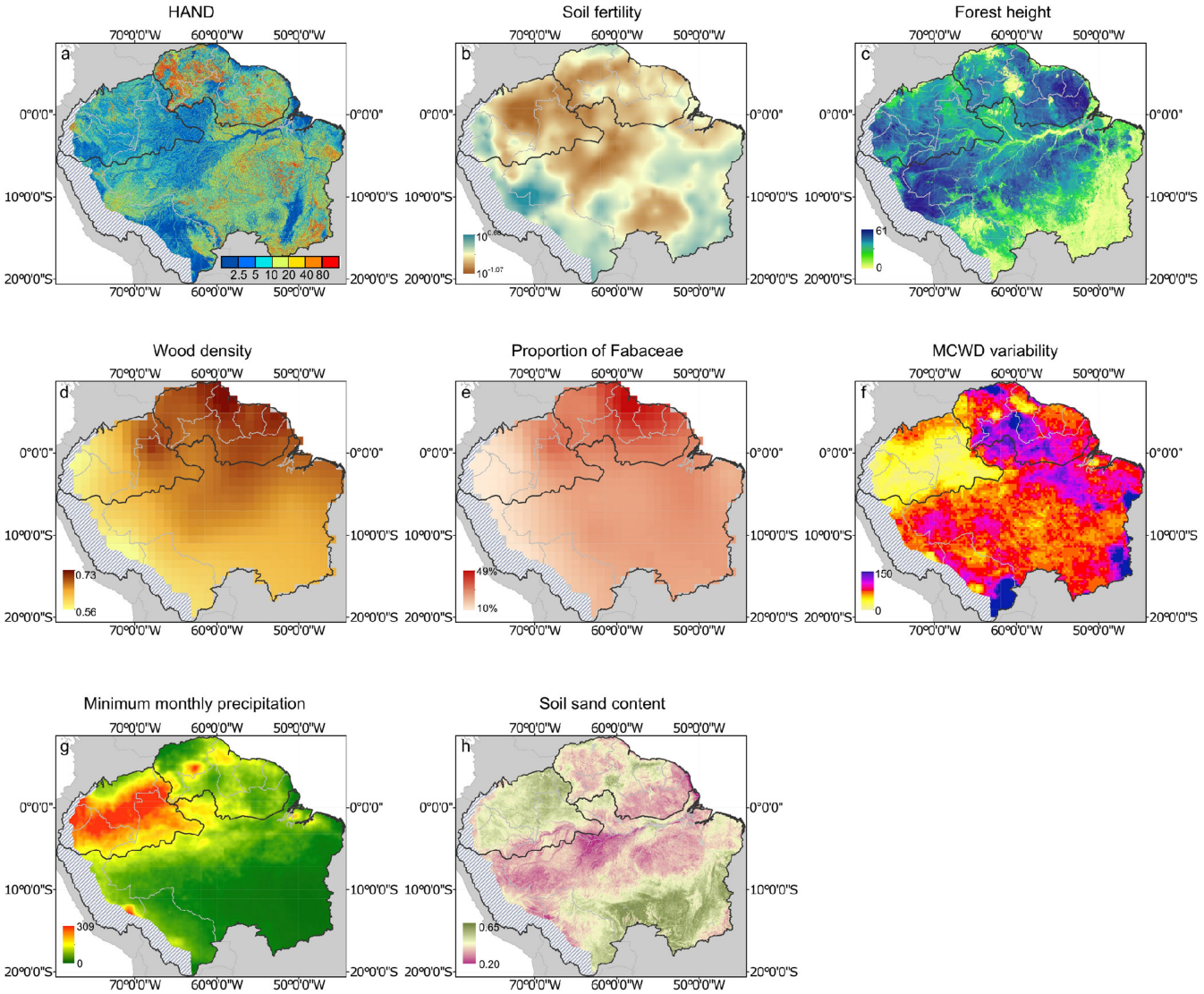

Extended Data Fig. 2 | Ecotope factors of the Amazon basin. (**a**) Height Above Nearest Drainage (HAND), a proxy for water-table depth[25]; (**b**) Soil fertility, as exchangeable base cation concentrations[43]; (**c**) Average forest heights as acquired by lidar[45]; (**d**) Soil sand content[44]; (**e**) Proportion of trees belonging to the Fabaceae family[34]; (**f**) MCWD variability (see the 'Climate anomalies for drought definition and mapping' section of methods), in terms of the standard deviation of the long-term MCWD timeseries. High variance in climate and low soil fertility in Guiana shield might contribute to the greatest proportion of trees belonging to the family Fabaceae with the very high wood density; (**g**) Averaged minimum monthly precipitation (low=green, high=orange). The north-west everwet Amazon is distinguished by lacking a dry season (precipitation exceeds evapotranspiration). (**h**) Community-weighted wood density[34]. Panels a-d are used as ecotope predictors in the GAM analysis of Supplementary Table 1. (Data sources: see the 'Climate variables' and 'Climate anomalies for drought definition and mapping' sections of methods).

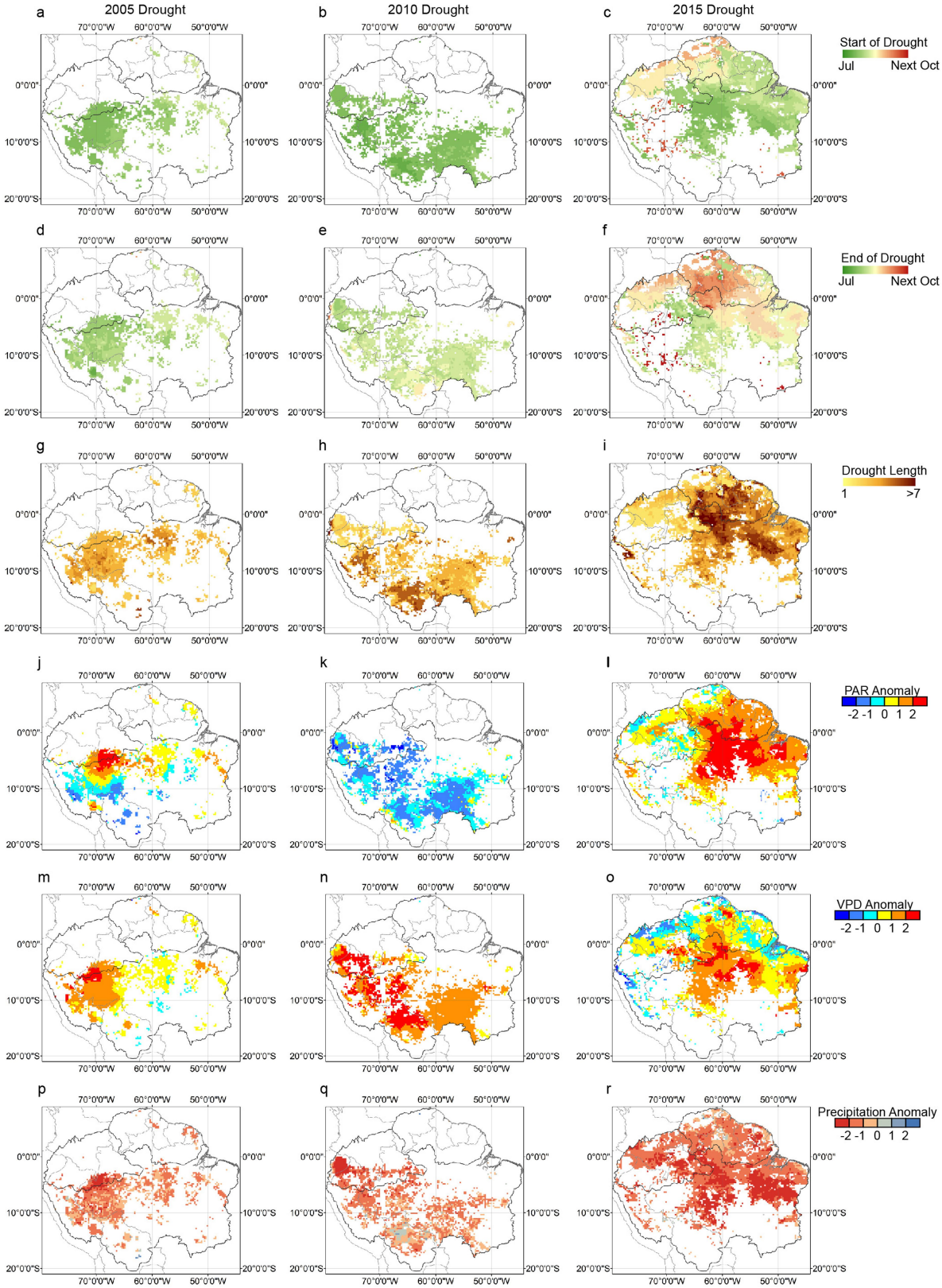

Extended Data Fig. 3 | Spatial distributions of climate dynamics in the 2005, 2010 and 2015 droughts. a–i, Spatial distributions of climate dynamics in the 2005 (left column), 2010 (middle column) and 2015 (right column) droughts for: (a)-(i): Drought dynamics showing drought onset date (row 1, a-c), drought end date (row 2, d-f), and drought duration (row 3, g-i, end date minus start date). Pixel-by-pixel drought responses (EVI in Figs. 1–4; or GOSIF in Extended Data Figs. 1 & 5) are taken as the standardized anomalies that occur during the pixel-specific drought period defined here. **(j)-(r): climatic anomalies** of: photosynthetic active radiation (PAR) (row 4, j-l), vapor pressure deficit (VPD) (row 5, m-o), and precipitation (row 6, p-r). precipitation (Data source: see the 'Climate variables' section of methods).

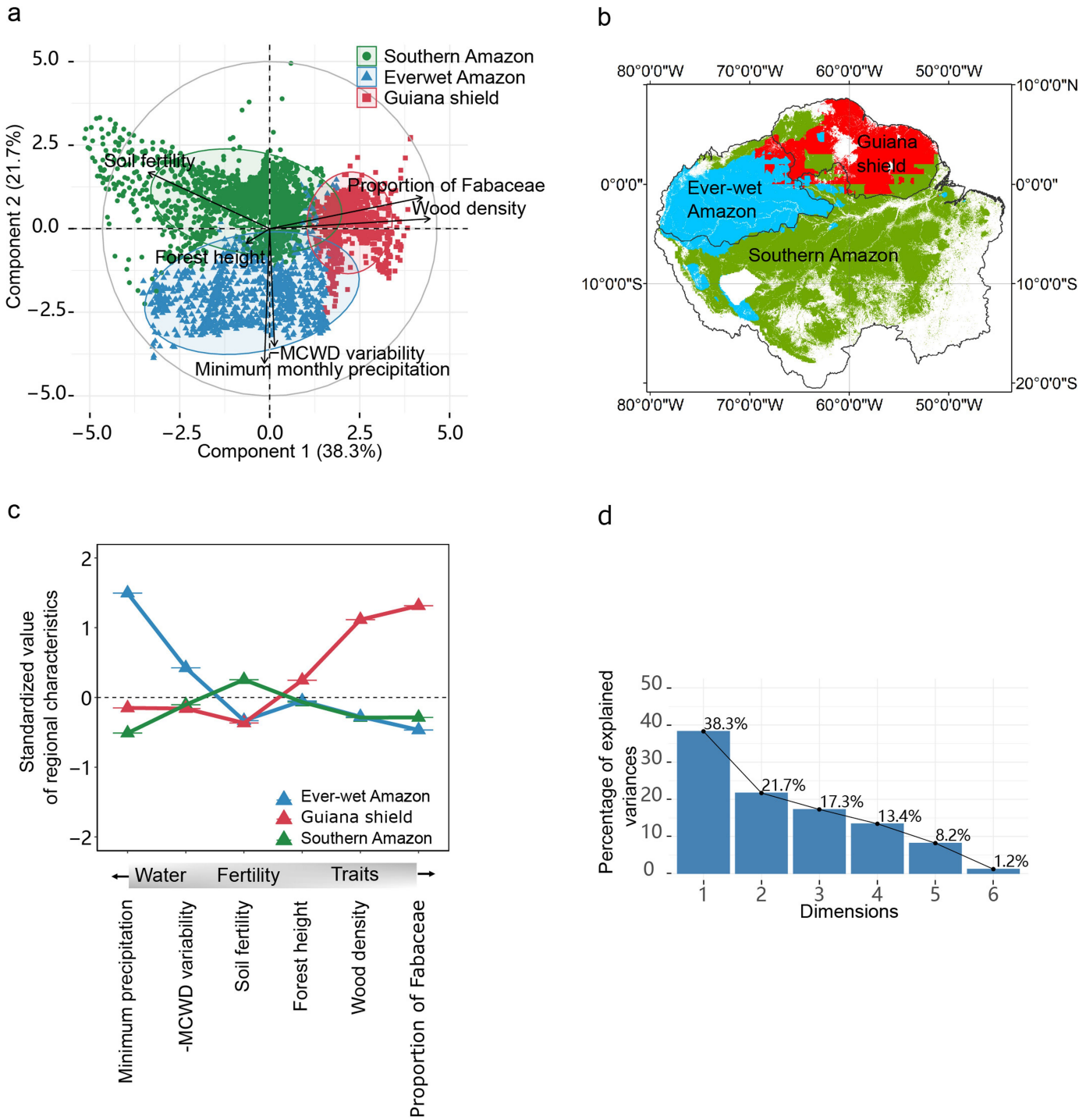

Extended Data Fig. 4 | Regions in the Amazon basin. that emerge from a principal components analysis (PCA) followed by classification: (**a**) PCA of the Amazon basin 0.4° x 0.4° pixel data (coloured according to a supervised classification into three classes identified by variance minimization), projected onto their first two principal components, which are composed mainly of three dimensions, one defined by wood density and proportions of the family Fabaceae (first principal component, horizontal axis), one defined by minimum monthly precipitation and MCWD variability (second principal component, vertical axis), and a third defined mainly by soil fertility; the classes are significantly separated in PCA space (psuedo-F ratio =950, df=2, 3805, p - 0, permanova test); (**b**) The Amazon pixels coloured according to their class (corresponding to the colours in a), showing that the classification of (a) maps pixels into distinct, mostly contiguous spatial regions.) (**c**) Standardized values, for each region, of each group of characteristics (ordered by water availability, soil fertility, and tree traits/characteristics), illustrate distinct regional niches: the everwet Amazon is highest in minimum precipitation and lowest (highest negative) in MCWD variability; the Southern Amazon is moderately high in mean fertility, and the Guiana Shield has the tallest mean forest height and greatest wood density. (**d**) scree plot of the eigenvalues (principal components) of the PCA shown in (a), plotted in rank order.

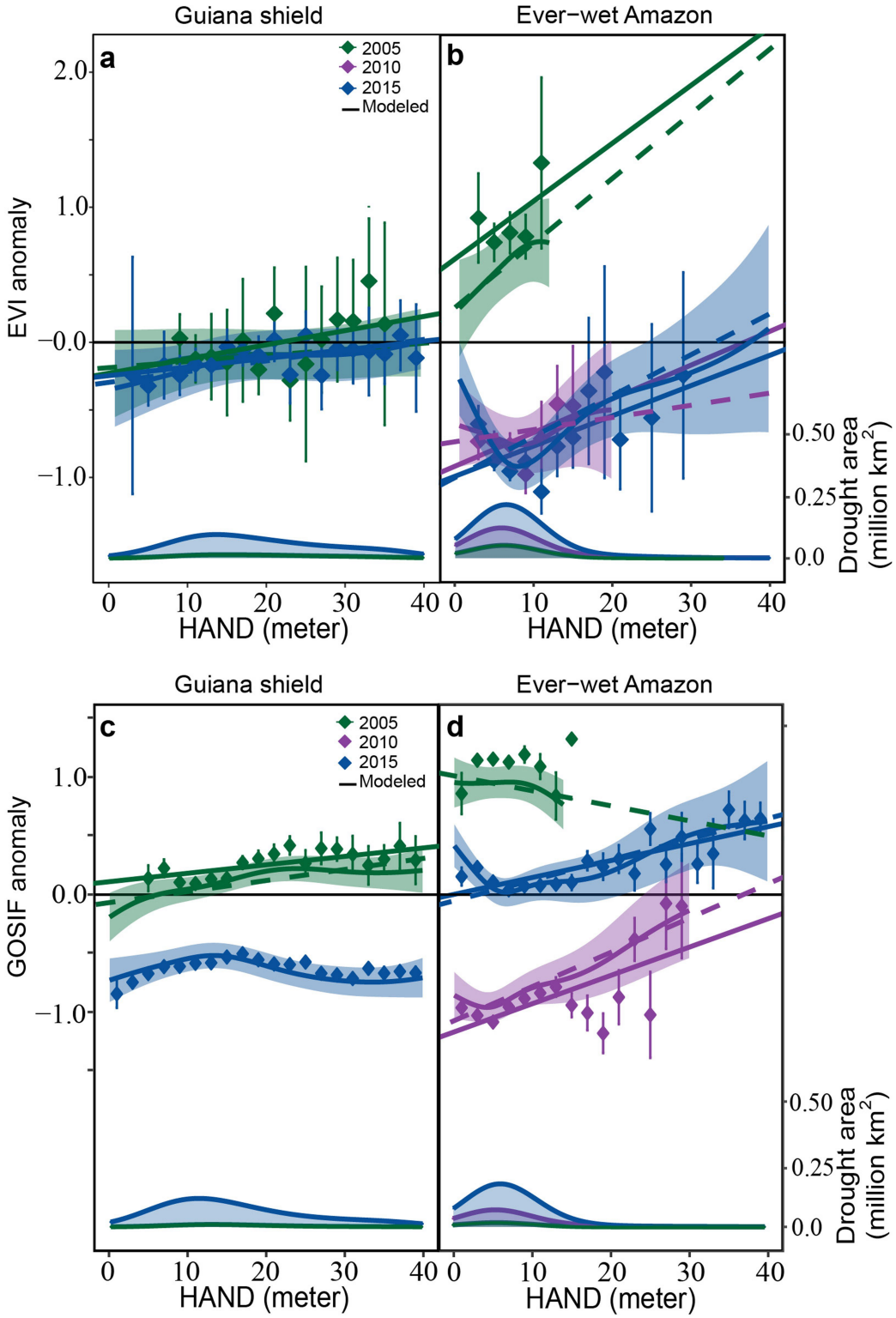

Extended Data Fig. 5 | Amazon forest drought responses in different regions using the EVI and GOSIF remote sensing indices. Amazon forest EVI (top row) and GOSIF (bottom row) responses to multiple droughts in the Guiana shield (left column) and the ever-wet northwest (right column). These generally do not support the "other side of drought" hypothesis 1, because they show generally consistently positive slopes with water-table depth (HAND), in contrast to negative slope responses in the Southern Amazon (Fig. 3a). Plots show observations (bin average points ±95% CI, and solid regression lines) and unified multi-drought GAM predictions (±95% CI shaded region, for models in Supplementary Table 1b, c), with climate fixed to region-wide median drought conditions for each drought.) Observations for EVI (a-b): N = 83 and 666 0.4° pixels for 2005 and 2015 droughts respectively, in the Guiana shield (a), and N = 147, 368, and 648 for 2005, 2010 and 2015 droughts respectively in the ever-wet Amazon (b). Observations for GOSIF (c-d): N = 1876, and 25,460 5-km pixels for 2005 and 2015 droughts, respectively, in Guiana shield (c), and N = 1,914, 8,261, and 19,918 for 2005, 2010 and 2015 droughts, respectively, in the ever-wet Amazon (d). Purple points (2010) are not shown in panels a,c, because the 2010 drought did not significantly affect the Guiana shield.

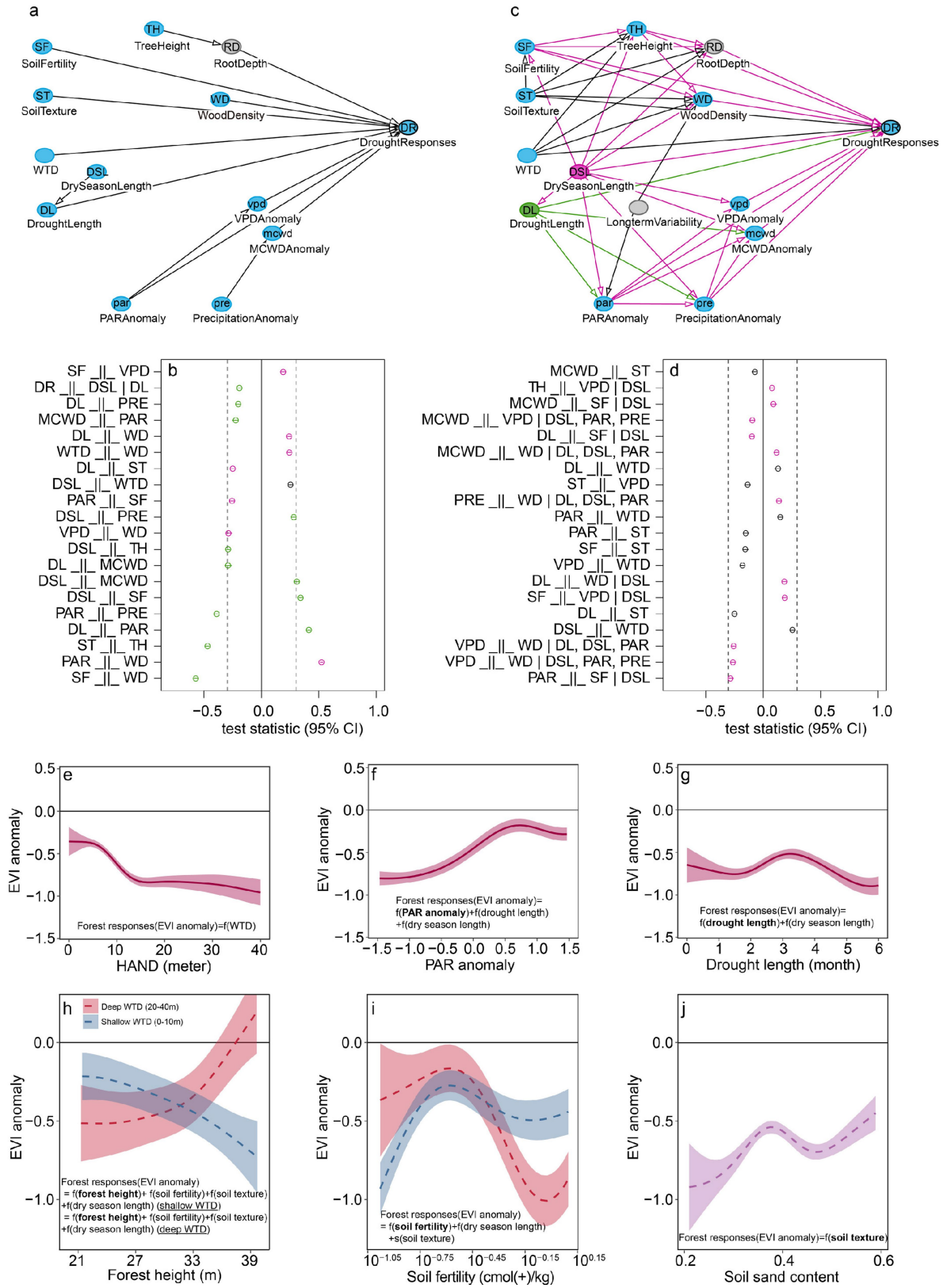

Extended Data Fig. 6 | See next page for caption.

Extended Data Fig. 6 | Implementing Structured Causal Modeling (SCM) of Amazon forest drought response using Directed acyclic graphs (DAGs). **a**–**d**, Development of a Directed acyclic graph (DAG) representing the structure of factors influencing tropical forest responses to drought. (**a**) Initially hypothesized DAG characterizing the causal relationships among climatic, environmental, and forest variables (measured variables depicted as blue nodes, unmeasured rooting depth is depicted in grey) leading to forest drought response (other colour node), with arrows representing the hypothesized causal links. (**b**) DAG-data consistency tests for initial DAG, with the largest 20 approximated non-linear correlation coefficients (estimated via root mean square error of approximation, RMSEA) between unlinked variables in (a). (Note: unlinked variables in a DAG are hypothesized to have zero correlation or zero conditional correlation; thus, the second row of panel b tests "DR_ | | _DSL | DL" -- whether DR is independent of DSL conditioned on DL, by estimating the non-linear correlation between DR and the residuals of DSL regressed on DL.) Correlations greater than an acceptability threshold (dashed vertical lines at ±0.30) fail the test of conditional independence, addressed by adding to the DAG either a direct causal link (indicated by a green symbol), or links to a common cause (pink symbol) (such added arrows are included in panel c). (**c**) Final DAG after correcting for conditional independency inconsistencies of the initial DAG in A, in light of ecological considerations. Also illustrates use of the backdoor criterion to determine the causal effect of 'drought length (DL)' (the exposed predictor node and associated forward causal paths, in green) on forest drought response (corresponding to the model in Extended Data Fig. 10c), while blocking the confounding variable dry season length, DSL (hypothesized to itself affect DL) and its associated causal backdoor paths (which are considered non-causal paths with respect to the exposed variable DL) (in pink). (**d**) DAG-Data consistency tests for final DAG (panel c), showing the largest 20 RMSEA values. **(e)-(j): GAM regression model predictions (±95% CI shaded region) of causal effects of different variables derived from DAG, employing backdoor criterion, for the Southern Amazon, average across all three droughts:** (**e**) of HAND (no backdoor to be blocked) (f) of PAR (adjusting for back door paths through drought length, dry season length) (**g**) of Drought length (adjusting for back door path through dry season length) on EVI responses (adjusted EVI prediction)**; the whole Amazon basin during the 2015 drought:** (**h**) of forest height, categorized by shallow (blue, HAND = 0-10 m) and deep (red, HAND = 20–40 m) water tables (adjusting for back door paths through soil fertility, soil texture and dry season length), (**i**) of soil fertility (adjusting for back door path through dry season length) (**j**) of soil texture (no backdoor path to be blocked).

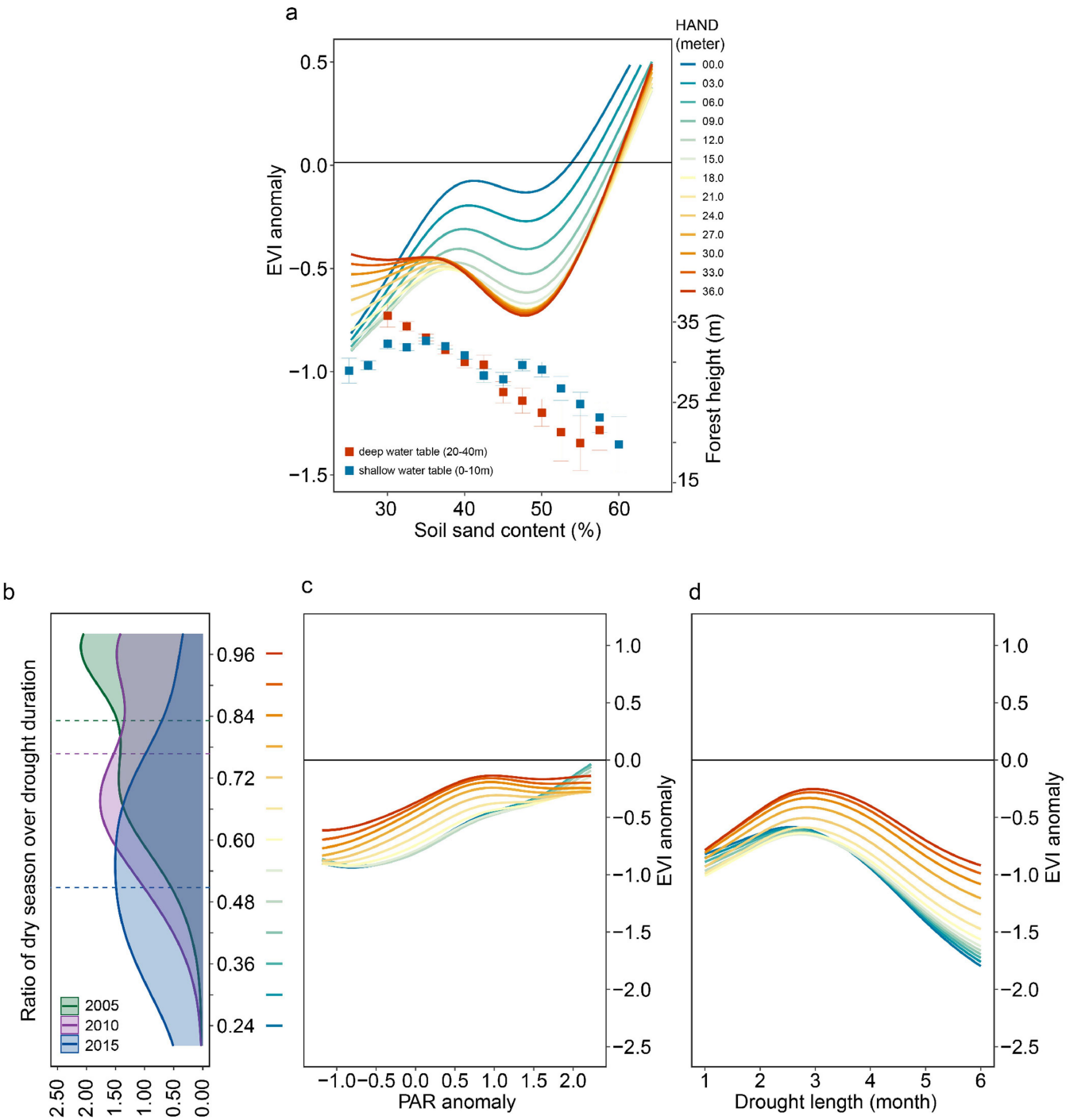

Extended Data Fig. 7 | The sensitivities of forest drought response to soil texture and drought timing. (**a**) The sensitivity of forest response to soil texture (sand content) and water-table depth (HAND) in basin-wide GAM analysis. GAM-predicted adjusted EVI anomaly (left axis) versus soil sand content (%), with water table-depth in colour (shallow=blue to deep=red), paired with distributions of mean forest height in each soil texture bin (bottom graph, right axis, with N = 3,318, and 1,142 0.4° pixels for shallow and deep water tables, respectively). 'Adjusted' GAM predictions are made by setting non-displayed predictors (climate variables, tree-height, soil fertility) to their median values during the drought. **(b)-(d): The sensitivity of forest responses to dry versus wet season drought periods, across the three-droughts:** (**b**) distribution of the proportion of drought that was in the dry season (0 = all in the wet season to 1= all in the dry season) for drought-affected pixels in each of the three droughts; (**c**) GAM-predicted EVI anomaly versus PAR, for different proportions of dry season drought (blue=all wet to red=all dry, corresponding to coloured tick marks in the vertical axis of b). (**d**) Adjusted EVI anomaly from GAM prediction versus drought length, for different proportions of dry-season drought (blue to red, as in panel c).

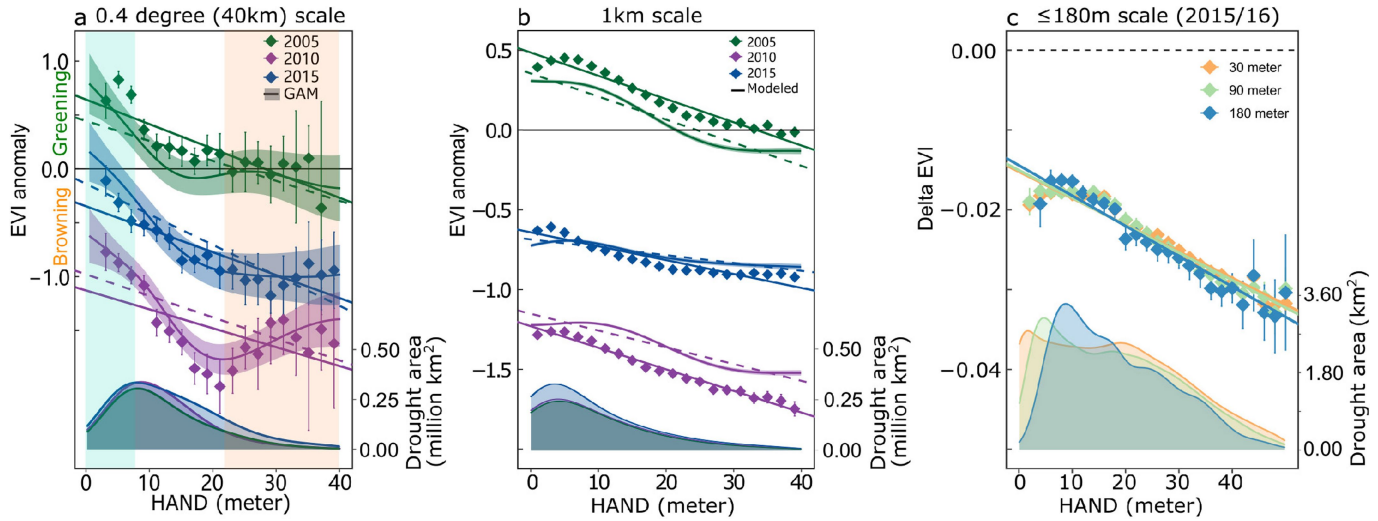

Extended Data Fig. 8 | Scale-dependence of Southern Amazon forest responses to drought, showing that detected response patterns are largely invariant across different scales of analysis. (**a**) At 0.4 degree (40-km) scale (across the Southern Amazon. all three droughts): Climate-adjusted EVI responses (standardized anomalies from MODIS) vs. water-table depths (indexed by HAND) for observations (solid points ±95% CI and solid regression line) and for unified multi-drought GAM predictions (model of Supplementary Table 1a, shaded bands and dashed regression line slopes) for the 2005 (green, slope = −0.019 ± 0.001 SE m^{-1}), 2010 (purple, slope = −0.020 ± 0.002 SE m^{-1}), and 2015 (blue, slope = −0.028 ± 0.002 SE m^{-1}) droughts (with N = 1,384, 1,673, and 1,837 0.4° pixels for 2005, 2010, and 2015 droughts, respectively); (**b**) At 1-km scale (across the Southern Amazon, all three droughts), as in (a): climate-adjusted EVI responses vs. HAND for observations (solid points and regression line) and corresponding GAM (with the same Supplementary Table 1a model now fit at 1 km scale, revealing autocorrelation in observations causing too-narrow confidence bands, and slight model underpredictions of the extremes of the 2005 greenup and the 2010 browdown, but maintaining the similar negative dependence on HAND across all droughts); (**c**) At 30 to 180 m scales (for a forest region around Manaus, 2015-2016 drought only): Delta EVI, the fraction change in EVI due to the drought = (after-drought EVI (July 2016) - pre-drought EVI (August 2015))/pre-drought EVI (Landsat OLI8, at 30 m resolution) vs. water-table depths (indexed by HAND) for Landsat observations (solid points ±95% CI and solid regression line) at native (30 m) and aggregated to 90 and 180-m scales (with N = 105,359, 11,901, and 2,999 pixels for 30-m, 90-m, and 180-m scales, respectively). Also shown in the bottom of each panel is the distribution of water-table depth (HAND proxy) at each scale. Aggregations to larger (coarser) scales induce an apparent regression towards the mean in the water-table depth distributions (as more extreme water-table depths at finer scales become diluted by averaging to large scales), while similar dilution of extremes in EVI response (not shown) preserves the overall relation between EVI responses and watertable depth (especially evident in the Landsat analysis where the slopes through data aggregated at different scales do not detectably differ).

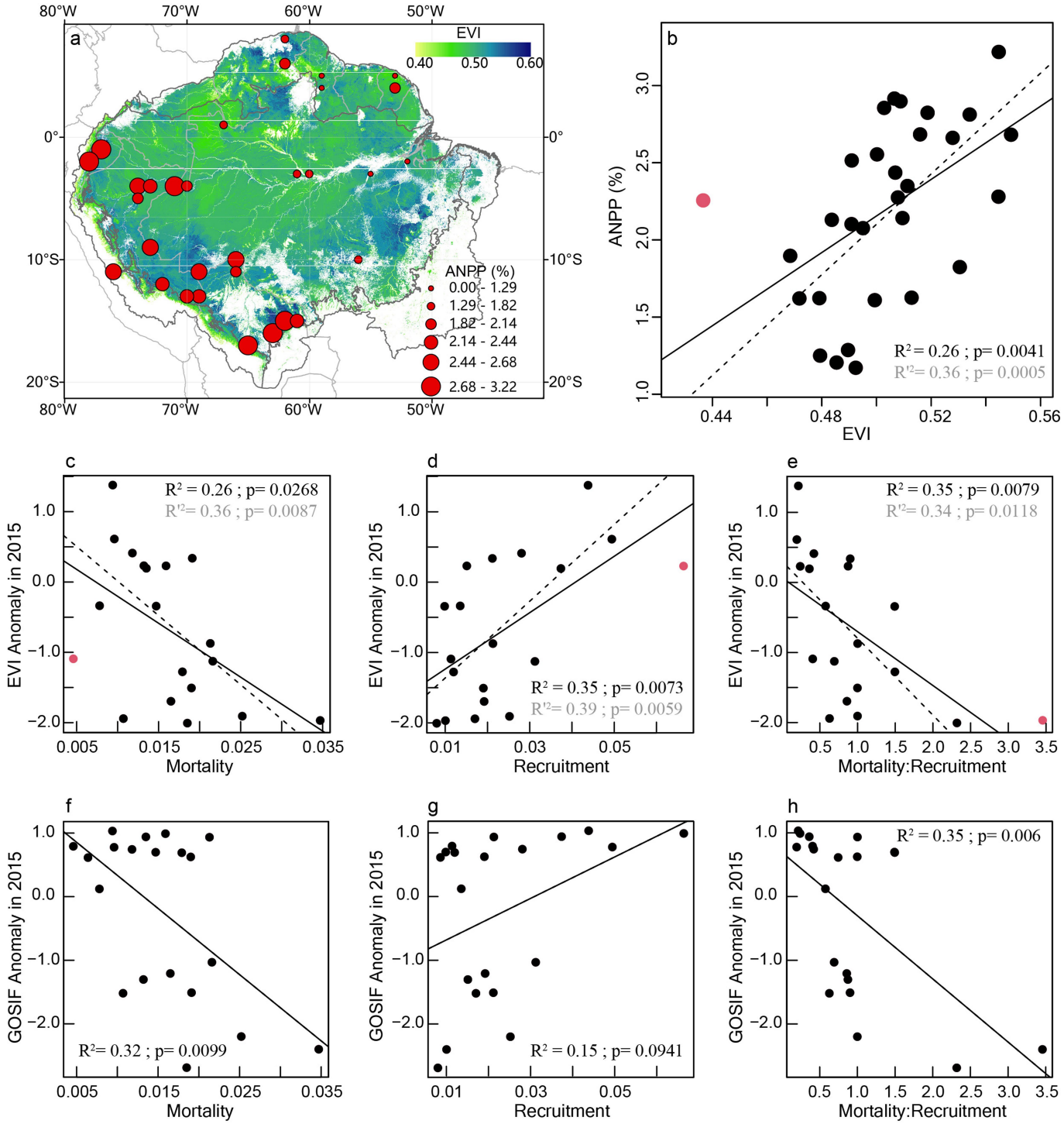

Extended Data Fig. 9 | See next page for caption.

Extended Data Fig. 9 | Remote sensing validation with forest inventory plot demography. (**a**) Remotely sensed map of MAIAC EVI (1-km resolution), overlaid with aboveground NPP (ANPP) rates from 321 ground-monitored forest plots (red circles, % standing biomass y^{-1}) as aggregated to 1 degree grid plots (RAINFOR plots in Brienen et al. [2]), with both EVI and ANPP taken during the 2000–2011 interval. ANPP rate is calculated as Aboveground Biomass (AGB) gain (Mg/(ha·yr)) (total annual AGB productivity of surviving trees plus recruitment, plus inferred growth of trees that died between censusing intervals) divided by initial AGB (Mg/ha) (standing above ground biomass at the start of the census interval). (**b**) **ANPP rates as predicted by EVI** (points from (a) plus solid regression line with statistics; Dashed line and associated statistics in grey represent linear regression without the high leverage point, shown in red, defined by Cook's distances > 4/n, where n=number of points[134]). EVI is the mean extracted from intervals matching the average census interval of the corresponding plots in Brienen et al. [2] **(c)–(e) MAIAC EVI anomalies (1-km pixels) versus ground-monitored tree demography in shallow water table forests during the 2015-2016 drought**[26] for: (c) mortality, (d) recruitment, and (e) mortality:recruitment ratios in 1-ha plots. **(f)–(h): GOSIF anomalies** (5-km pixels) versus ground-monitored (f) mortality, (g) recruitment, and (h) mortality:recruitment ratios; Solid lines and statistics (R^2 and p-values) represent standard linear regression fits to all data. Red points, if they exist, are high leverage, i.e. with Cook's distances > 4/n, where n=number of points[134], and dotted lines and associated statistics in grey represent standard linear regressions without such points, showing that remote detection of ground-derived demographic trends is robust. R^2 values reported here are consistent with the expectation that they should be less than for remote detection of tropical forest GPP (R^2 = 0.5-0.7), because GPP contributes only partially to the NPP driver of demography (as discussed in the 'Validation by forest plot metrics of demography and of physiological drought tolerance' section of Methods). Considering multple comparisons (six regressions), the probability, under the null hypothesis, of seeing five or more significant regresssions out of six is p = 0.000002 (Binomial test).

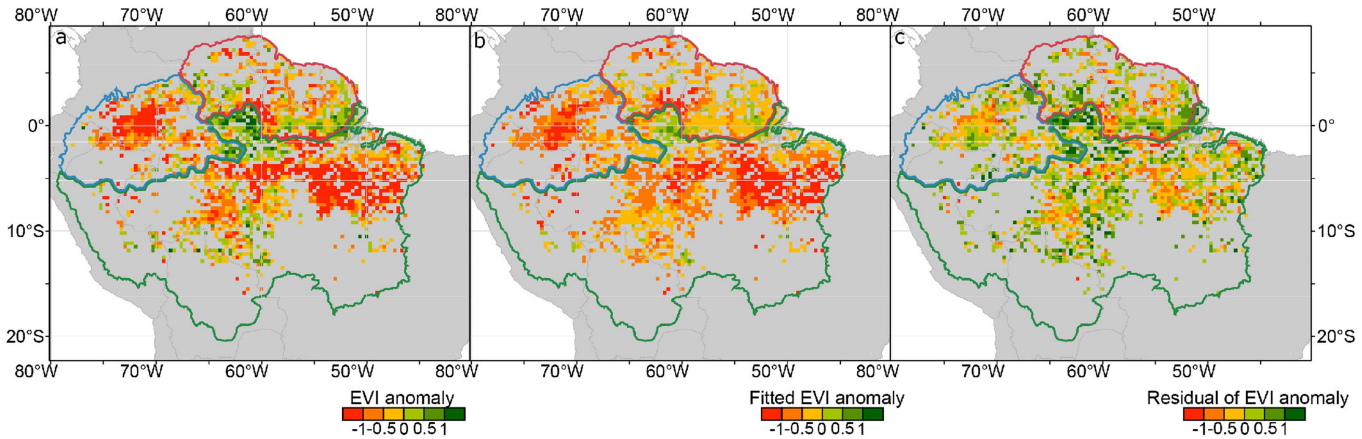

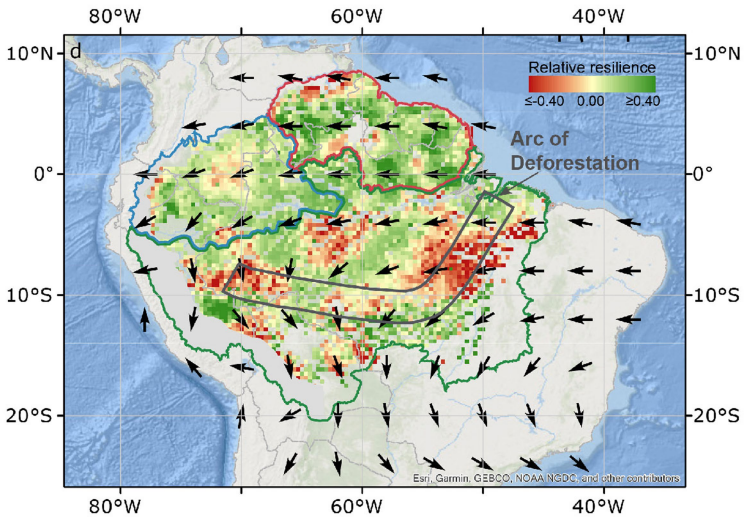

Extended Data Fig. 10 | Modeled forest response to the 2015 drought and implications of the derived map of Amazon forest biogeography. **a**–**c**, Forest response to the 2015 drought in drought-affected pixels. (**a**) Observed EVI anomalies (resampled at 0.4 degrees to match model resolution which accounts for spatial autocorrelation (see Supplementary Fig. 1). (**b**) GAM-predicted EVI anomalies (model of Supplementary Table 1d). (**c**) Residual EVI anomalies (panel a observations minus panel b predictions). The GAM well-predicts the pattern of response (Panel b), but under-estimates the extremes of the responses (as evident from residuals in panel c continuing to show greening/browning patterns beyond the predictions). (**d**) **Map of Amazon forest biogeography of resilience/vulnerability, overlaid with mean winds (arrows, at height 650 hPa) and location of the arc of deforestation.** The most productive as well as the most vulnerable forests (in red) are also those most experiencing deforestation (in the "arc of deforestation") which is causing local climatic warming/drying[4], further stressing these vulnerable forests. These "arc of deforestation"/vulnerable forests are often upwind forests[135] (especially when the Intertropical convergence zone, ITCZ, swings to the south) that are critical for hydrological recycling in the Amazon.

nature portfolio

Corresponding author(s): Shuli Chen, Scott Saleska

Last updated by author(s): Mar 26, 2024

Reporting Summary

Nature Portfolio wishes to improve the reproducibility of the work that we publish. This form provides structure for consistency and transparency in reporting. For further information on Nature Portfolio policies, see our Editorial Policies and the Editorial Policy Checklist.

Statistics

For all statistical analyses, confirm that the following items are present in the figure legend, table legend, main text, or Methods section.

n/a	Confirmed	
☐	☒	The exact sample size (*n*) for each experimental group/condition, given as a discrete number and unit of measurement
☐	☒	A statement on whether measurements were taken from distinct samples or whether the same sample was measured repeatedly
☐	☒	The statistical test(s) used AND whether they are one- or two-sided *Only common tests should be described solely by name; describe more complex techniques in the Methods section.*
☐	☒	A description of all covariates tested
☐	☒	A description of any assumptions or corrections, such as tests of normality and adjustment for multiple comparisons
☐	☒	A full description of the statistical parameters including central tendency (e.g. means) or other basic estimates (e.g. regression coefficient) AND variation (e.g. standard deviation) or associated estimates of uncertainty (e.g. confidence intervals)
☐	☒	For null hypothesis testing, the test statistic (e.g. *F*, *t*, *r*) with confidence intervals, effect sizes, degrees of freedom and *P* value noted *Give P values as exact values whenever suitable.*
☒	☐	For Bayesian analysis, information on the choice of priors and Markov chain Monte Carlo settings
☐	☒	For hierarchical and complex designs, identification of the appropriate level for tests and full reporting of outcomes
☐	☒	Estimates of effect sizes (e.g. Cohen's *d*, Pearson's *r*), indicating how they were calculated

Our web collection on statistics for biologists contains articles on many of the points above.

Software and code

Policy information about availability of computer code

Data collection	No software was used in data collection.
Data analysis	Data was analyzed and visualized with a custom code using R (4.2.0 and earlier) and the following R packages (mgcv 1.9-1, dagitty 0.3-1, ggplot2 3.4.4, FactoMineR 2.4 etc), as well as in ENVI 5.3 + IDL8.5, Matlab2018b. Geographical maps were processed in ArcGIS 10.6.1. Custom code for data processing for the figures, and for fitting the statistical models (GAM and DAG models) are deposited in a community repository (Code Ocean) according to Nature guidelines. Code for reproducing the modeling analysis and figures is posted on Code Ocean at https://codeocean.com/capsule/2432086/tree.

For manuscripts utilizing custom algorithms or software that are central to the research but not yet described in published literature, software must be made available to editors and reviewers. We strongly encourage code deposition in a community repository (e.g. GitHub). See the Nature Portfolio guidelines for submitting code & software for further information.

Data

Policy information about availability of data

All manuscripts must include a data availability statement. This statement should provide the following information, where applicable:

- Accession codes, unique identifiers, or web links for publicly available datasets
- A description of any restrictions on data availability
- For clinical datasets or third party data, please ensure that the statement adheres to our policy

All remote sensing data and products (vegetation/photosynthetic indices(https://lpdaac.usgs.gov/products/mcd19a3v006/, http://data.globalecology.unh.edu/data/GOSIF_v2), climate variables (https://disc2.gesdisc.eosdis.nasa.gov/data/TRMM_L3/TRMM_3B43.7/, https://goldsmr4.gesdisc.eosdisc.nasa.gov/data/MERRA2_MONTHLY/M2TMNXRAD.5.12.4/, https://airs.jpl.nasa.gov/data/get-data/standard-data/), land cover (https://lpdaac.usgs.gov/products/mcd12q1v006/, https://forobs.jrc.ec.europa.eu/TMF), tree characteristics (canopy height https://webmap.ornl.gov/ogc/dataset.jsp?dg_id=10023_1), soil texture (https://maps.isric.org/)) are publicly available at the website locations cited in the methods. The ground-based demographic validation data is publicly available in the method to Sousa et al. (2020; see References), and Brienen et al. (2015; see References). The ground-based hydraulic trait validation data is publicly available in the method to Tavares et al. (2023; see References). The HAND data are derived from digital elevation model-Shuttle Radar Topography Mission in Nobre et al. (2011; see References). The soil fertility data is available in Zuquim et al. (2019; see References).

Research involving human participants, their data, or biological material

Policy information about studies with human participants or human data. See also policy information about sex, gender (identity/presentation), and sexual orientation and race, ethnicity and racism.

Reporting on sex and gender	NA
Reporting on race, ethnicity, or other socially relevant groupings	NA
Population characteristics	NA
Recruitment	NA
Ethics oversight	NA

Note that full information on the approval of the study protocol must also be provided in the manuscript.

Field-specific reporting

Please select the one below that is the best fit for your research. If you are not sure, read the appropriate sections before making your selection.

☐ Life sciences ☐ Behavioural & social sciences ☒ Ecological, evolutionary & environmental sciences

For a reference copy of the document with all sections, see nature.com/documents/nr-reporting-summary-flat.pdf

Ecological, evolutionary & environmental sciences study design

All studies must disclose on these points even when the disclosure is negative.

Study description	This study models forest responses to three 'once in a century' droughts using satellite vegetation indices and ground-based demographic data to go beyond climate-only explanations, to test three hypotheses for how climate interacts with different forest 'ecotypes' to explain the complexity of forest drought response at multiple scales. Two basic approaches taken in forest drought research have been: remote sensing explorations of drought-induced vegetation greening/browning patterns and how they correlate with climate across landscapes (but without much mechanistic biology); and ground- based studies of biological mechanisms of individual tree resilience or of plot-scale tree demography (but with limited connection to the heterogeneity of the broader landscape). Our study takes a novel approach that uniquely integrates both approaches, using remote sensing to test and then constrain region- to basin-scale implications of recent ecological hypotheses. The study shows how forest responses to drought are structured across landscapes, according to ecotype factors (water-table depth, soil fertility, and tree community characteristics) that are conducive (or not) to drought resilience. Our results provides new insight (and a warning) about which forests may be vulnerable, and which resilient, to future droughts.
Research sample	Well-validated satellite vegetation indices of photosynthetic capacity (the Enhanced Vegetation Index, EVI) and photosynthetic activity (the Global OCO-2 Solar Induced Fluorescence, GOSIF) were sampled over 19 hydrological years across the whole basin constrained by evergreen forests. The EVI is sampled as 8-day and aggregated to a monthly time step while GOSIF is sampled as monthly. Climate and ecotope observations were sampled to match the corresponding remotely sensed vegetation observations. The ground-based demographic forest tree samples from Brienen at al. (2015; see References) are as described in the reference individual trees > 10cm in diameter at breast height sampled and measured over 28 years from 321 tree plots of RAINFOR and other networks, which are distributed through regions of the Amazon basin). The mortality and recruitment demographic data from Sousa

	et al (2020; see References) are as described in the reference (observations of approximately 15,000 trees from two censuses during dry season in 2015 and 2016 with 25 1-ha plots). A pan-Amazon hydraulic trait dataset (hydraulic safety margins) from Tavares et al (2023; see References) are as described in the reference (sampled across 9 forest sites, including 108 species, distributed across western, central eastern and southern Amazon, sampling species representing between 14% and 70% of the total basal area).
Sampling strategy	We only sampled observations in evergreen forest type from non-flooded areas with cloud-free and low aerosol conditions. For statistical modeling we interpolated different datasets to common grid resolutions, according to the desired resolution of the model. This was typically 0.4°, the resolution needed to avoid inflation of statistical significance of drought responses in models by accounting for spatial autocorrelation among nearby pixels using variogram analysis.
Data collection	All remote sensing and ground-based demographic/hydraulic trait raw data and products are collected and processed by researchers at the website locations cited in the supplementary methods.
Timing and spatial scale	The remote sensed vegetation observations (1-km) are across 19 hydrological years of 2000-2020 (May 2000 to April 2020) at a monthly step across the whole basin constrained by drought region. The published demographic datasets from Brienen at al. (2015; see References) are over the period 1983-2011 from 321 tree plots of the RAINFOR and other networks, while the mortality and recruitment data from Sousa et al (2020; see References) are collected from two censuses during dry season in 2015 and 2016 with 25 1-ha plots distributed across eight research sites along the BR-319 road in the southern Amazon between Manaus and Porto Velho. A pan-Amazon hydraulic trait dataset (hydraulic safety margins) from Tavares et al (2023; see References) are sampled across 9 forest sites distributed across western, central eastern and southern Amazon over the period of 2014-2018.
Data exclusions	We excluded observations belonging to open water, deforested forests, and non-forest vegetation types, but only included evergreen forests. We also excluded floodplain from non-flooded forests, as well as excluded observations with cloud/aerosol contaminations. We conducted a sensitivity test by excluding majority or the entirety of degraded forests.
Reproducibility	The study is not based on experiments.
Randomization	This is not relevant to the study, as no experiments were performed.
Blinding	Blinding was not necessary as we did not perform any experiment containing groups and/or treatments, but analyzed long-term vegetation indices and demographic/hydraulic trait data for which blinding is not required.

Did the study involve field work? ☐ Yes ☒ No

Reporting for specific materials, systems and methods

We require information from authors about some types of materials, experimental systems and methods used in many studies. Here, indicate whether each material, system or method listed is relevant to your study. If you are not sure if a list item applies to your research, read the appropriate section before selecting a response.

Materials & experimental systems

n/a	Involved in the study
☒	☐ Antibodies
☒	☐ Eukaryotic cell lines
☒	☐ Palaeontology and archaeology
☒	☐ Animals and other organisms
☒	☐ Clinical data
☒	☐ Dual use research of concern
☒	☐ Plants

Methods

n/a	Involved in the study
☒	☐ ChIP-seq
☒	☐ Flow cytometry
☒	☐ MRI-based neuroimaging

Plants

Seed stocks	NA
Novel plant genotypes	NA
Authentication	NA